nature photonics

Supplementary information

https://doi.org/10.1038/s41566-025-01780-4

Electrical control of photon spin angular momentum in organic electroluminescent materials

In the format provided by the authors and unedited

Table of Contents

Synthesis and characterisation of 4-fluoro[6]helicene (monoF[6]H)

General: Melting points were determined on Mikro-Heiztisch Polytherm A (Hund, Wetzlar) apparatus and are uncorrected. The NMR spectra were measured on Bruker Advance III HD 400 instrument. The ^{1}H NMR spectra were measured at 400.13 MHz, the ^{19}F NMR spectra at 376.46 or 377.28 MHz, the ^{13}C NMR spectra at 100.61 MHz in $CDCl_3$ as indicated in 5 mm PFG probe with indirect detection. For standardisation of ^{1}H NMR spectra the residual signals of solvent (δ 7.26 for $CHCl_3$) was used. In the case of ^{13}C spectra the signal of solvent (δ 77.16 for $CDCl_3$) was used. The chemical shifts are given in *δ*-scale, the coupling constants *J* are given in Hz. The IR spectra were measured in $CHCl_3$. The EI mass spectra were determined at an ionising voltage of 70 eV, the *m/z* values are given along with their relative intensities (%). The standard 70 eV spectra were recorded in the positive ion mode. The sample was dissolved in chloroform, loaded into a quartz cup of the direct probe and inserted into the ion source. The source temperature was 220 °C. For exact mass measurement, the spectrum was internally calibrated using perfluorotri-*n*-butylamine (Heptacosa). The ECD and absorption spectra of molecules in solution were measured on a Jasco 1500 spectropolarimeter (JASCO International Co. Ltd.) equipped with a fluorescence emission monochromator (FMO522) and separate fluorescence emission detector (FDT-538). The ECD and absorption spectra were measured over a spectral range of 210 nm to 550 nm in tetrahydrofuran (10^{-4} M solutions). Measurements were made in quartz cell with a 0.1 cm path length using a scanning speed of 20 nm/min, a response time of 4 s, and standard instrument sensitivity. After a baseline correction, spectra were expressed in terms of differential molar extinction (Δε) and molar extinction (ε), respectively. Optical rotations were measured in $CHCl_3$ using an Autopol IV instrument (Rudolph Research Analytical). For analytical separations (CSP screening, optimisation and determination of enantiomeric excess), a high-pressure gradient HPLC system (Knauer Azura) with diode array (200-800 nm, Knauer) and polarimetric (Chiralyser, IBZ Messtechnik) detectors was used. For semi-preparative resolutions, Puriflash PF5.250 (Interchim) combined Flash/HPLC chromatograph equipped with a diode array detector (200-800 nm) was used. HPLC grade solvents (Avantor) were used for all HPLC separations.

TLC was performed on Silica gel 60 F_{254}-coated aluminium sheets (Merck) and spots were detected by the solution of $Ce(SO_4)_2$. 4 H_2O (1%) and $H_3P(Mo_3O_{10})_4$ (2%) in sulfuric acid (10%). The flash chromatography was performed on Silica gel 60 (0.040-0.063 mm, Fluka) on Biotage® KP-C18-HS using the Isolera One HPFC system (Biotage, Inc.). Biotage Initiator EXP EU (300 W power) was used for reactions carried out in a microwave oven. Microwave reactions were performed in sealed reaction vessels (containing a pressure relief septum). Triethylamine was distilled from calcium hydride under nitrogen; tetrahydrofuran was freshly distilled from sodium/benzophenone under nitrogen. Otherwise, all commercially available solvents, catalysts and reagent grade materials were used as received.

The starting material 2-bromo-6-fluorobenzaldehyde **1** was purchased, CpCo(CO)(fum) (fum = dimethyl fumarate)[1] and aldehyde **2**[2] were synthesized according to the literature procedure.

Synthesis of 4-fluoro[6]helicene (monoF[6]H)

Figure S1: Synthesis of 4-fluoro[6]helicene (monoF[6]H).

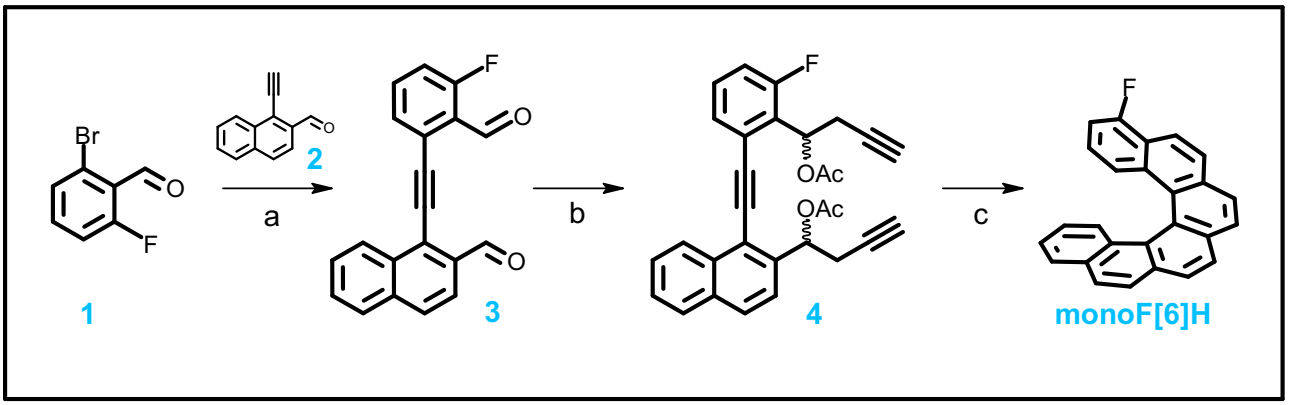

(a) (2) (1.1 equiv.), $Pd(PPh_3)_2Cl_2$ (2 mol%), CuI (4 mol%),THF-Et_3N (3:1), 50 °C, 4 h, 80%; (b) $BrCH_2$-C≡CH (5.0 equiv.), Zn (5.0 equiv.), THF, rt, 5 min, then Et_3N (6.0 equiv.), Ac_2O (6.0 equiv.), rt, 3 h, 67%; (c) CpCo(CO)(fum) (0.3 equiv.), PhCl, μW, 170 °C, 20 min, then *p*-TsOH (5.0 equiv.), 95 °C, 1 h, 70%.

a) 1-[(3-Fluoro-2-formylphenyl)ethynyl]naphthalene-2-carbaldehyde (3)

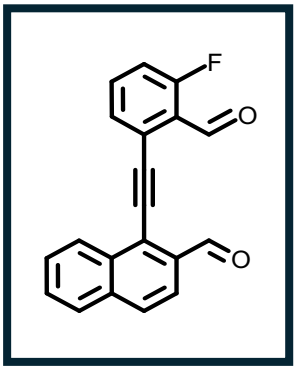

A Schlenk flask was charged with aldehyde (1) (1.00 g, 4.93 mmol), $Pd(PPh_3)_2Cl_2$ (69.2 mg, 0.10 mmol, 2 mol%), CuI (37.6 mg, 0.20 mmol, 4 mol%) and flushed with nitrogen. The degassed tetrahydrofuran (10 ml) and the degassed triethylamine (5 ml) were added and the mixture was heated to 50 °C. Then alkyne (2) (977 mg, 5.42 mmol, 1.1 equiv.) in degassed tetrahydrofuran (5 ml) was slowly added and the reaction was stirred at 50 °C for 4 h. The solvents were evaporated under the reduced pressure and the residue was purified by flash chromatography on silica gel (hexane-ethyl acetate 20:1 to 6:1) to get dialdehyde (3) (1.19 g, 80%) as a white crystalline solid.

M.p.: 110-111 °C (dichloromethane).

^{1}H NMR (400 MHz, $CDCl_3$): 7.21 – 7.28 (m, 1H), 7.59 – 7.66 (m, 2H), 7.67 – 7.76 (m, 2H), 7.91 (dd, *J* = 7.3, 1.5, 1H), 7.93 (d, *J* = 8.4, 1H), 8.00 (d, *J* = 8.6, 1H), 8.78 (ddt, *J* = 8.3, 1.5, 0.8, 1H), 10.64 (s, 1H), 10.95 (d, *J* = 0.8, 1H).

^{19}F NMR (377 MHz, $CDCl_3$): -118.31 (dd, *J* = 11.2, 3.6).

^{13}C NMR (101 MHz, $CDCl_3$): 89.70, 98.64 (d, *J* = 4.4), 117.55 (*J* = 21.6), 122.31, 124.32 (d, *J* = 3.4), 124.45 (d, *J* = 8.1), 126.37, 127.57, 128.28, 128.62, 129.66, 130.03, 130.65 (d, *J* = 3.5), 133.53, 135.26 (d, *J* = 10.6), 135.28, 135.87, 164.57 (d, *J* = 260.5), 186.70 (d, *J* = 7.3), 192.27 (d, *J* = 1.9).

IR ($CHCl_3$): 3062 w, 2847 m, 2780 w, 2197 vw, 1696 vs, 1678 m, 1618 w, 1601 m, 1592 w, 1568 m, 1473 m, 1458 w, 1433 w, 1387 w, 1266 w, 1240 m, 1228 m, 1196 w, 1154 w, 1075 w, 1028 w, 824 m, 715 w, 535 w cm^{-1}.

EI MS: 302 ($M^{+\bullet}$, 100), 273(28), 246 (76), 224 (10), 151 (12), 136 (11), 122 (28), 113 (12).

HR EI MS: calculated for $C_{20}H_{11}FO_2$ 302.0738, found 302.0738.

b) 1-[1-({2-[1-(Acetyloxy)but-3-yn-1-yl]-3-fluorophenyl}ethynyl)naphthalen-2-yl]but-3-yn-1-yl acetate (4)

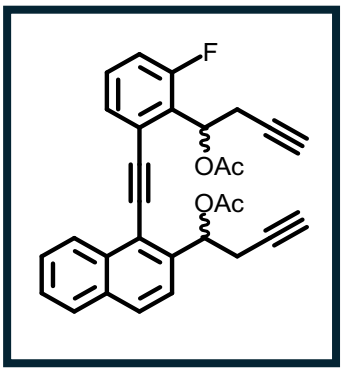

A Schlenk flask was filled with zinc powder (870 mg, 13.3 mmol, 5.0 equiv.) and flushed with nitrogen. Freshly distilled tetrahydrofuran (8 ml) was added, the suspension was placed into water bath (at room temperature) and vigorously stirred. Then propargyl bromide (80 wt.% in toluene, 2.53 ml, 13.3 mmol, 5.0 equiv.) was added within 10 min and the mixture was then stirred at room temperature for 20 min, before it was transferred by a syringe to the second Schlenk flask with dialdehyde (3) (800 mg, 2.65 mmol) in tetrahydrofuran (20 ml). The reaction mixture was stirred at room temperature for 5 min, then triethylamine (2.22 ml, 15.9 mmol, 6.0 equiv.) and acetic anhydride (1.50 ml, 15.9 mmol, 6.0 equiv.) were added and the solution was stirred at room temperature for 3 h. The mixture was evaporated under the reduced pressure to dryness. The residue was purified by flash chromatography on silica gel (hexane-ethyl acetate 10:1 to 7:1) to obtain (4) (828 mg, 67%) as an amorphous solid.

^{1}H NMR (400 MHz, $CDCl_3$, mixture of diastereomers): 2.00 – 2.03 (m, 4H), 2.097 (s, 3H), 2.104 (s, 3H), 2.18 (s, 6H), 2.90 – 3.23 (m, 8H), 6.60 (td, *J* = 7.6, 0.9, 1H), 6.61 (td, *J* = 7.6, 0.9, 1H), 6.70 – 6.76 (m, 2H), 7.11 (ddd, *J* = 10.5, 8.3, 1.2, 2H), 7.35 (ddd, *J* = 8.3, 7.7, 5.5, 2H), 7.52 (m, 4H), 7.61 – 7.68 (m, 4H), 7.86 (ddd, *J* = 8.1, 1.4, 0.7, 2H), 7.90 (d, *J* = 8.6, 2H), 8.59 – 8.64 (m, 2H).

^{19}F NMR (377 MHz, $CDCl_3$): -114.64 (dd, *J* = 10.1, 5.4).

^{13}C NMR (101 MHz, $CDCl_3$, mixture of diastereomers): 21.01 (2C), 21.21 (2C), 24.01 (d, *J* = 2.7), 24.04 (d, *J* = 2.9), 25.94, 25.97, 69.50, 69.61, 70.88, 70.90, 70.97, 71.04, 72.16, 72.27, 79.26 (2C), 79.52, 79.60, 90.48 (2C), 97.36 (d, *J* = 4.2), 97.40 (d, *J* = 4.0), 116.81 (d, *J* = 22.7, 2C), 118.41, 118.47, 123.11, 123.18, 124.39 (d, *J* = 5.6), 124.42 (d, *J* = 5.7), 126.79, 126.83, 126.95 (2C), 127.10, 127.11, 127.54 (2C), 128.30 (2C), 129.44, 129.46, 129.53 (d, *J* = 3.4, 2C), 129.99 (d, *J* = 9.7), 130.01 (d, *J* = 9.6), 132.87 (2C), 133.39, 133.41, 139.90, 139.94, 161.18 (d, *J* = 249.6, 2C), 169.93, 169.95, 170.07, 170.11.
IR ($CHCl_3$): 3309 m, 3062 w, 2960 vw, 2922 w, 2854 vw, 2202 vw, 2125 vw, 1742 vs, 1608 w, 1593 w, 1575 w, 1509 w, 1473 w, 1458 w, 1434 w, 1422 w, sh, 1241 vs, 1201 w, 1161 vw, 1151 vw, 1045 m, 1030 m, 911 w, 822 m, 652 m, 640 m, 606 w, 553 w cm^{-1}.
EI MS: 466 ($M^{+\bullet}$, 2), 363(8), 346 (29), 325 (100), 296 (58), 276 (29), 257 (12), 43 (45).

HR EI MS: calculated for $C_{30}H_{23}FO_4$ 466.1575, found 466.1570.

c) 4-Fluoro[6]helicene (monoF[6]H)

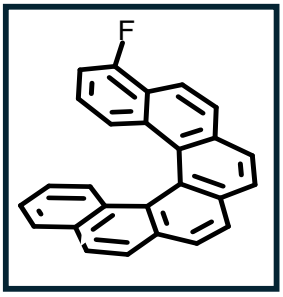

A crimp-sealed pressure vial was charged with triyne (4) (800 mg, 1.71 mmol) and chlorobenzene (24 ml) was added. The solution was bubbled with nitrogen for 10 min before CpCo(CO)(fum) (152 mg, 0.51 mmol, 0.3 equiv., fum = dimethylfumarate) was added. The vial was sealed and the reaction mixture was heated to 170 °C in the microwave reactor for 20 min. The reaction mixture was transferred to a flask, *p*-toluenesulfonic acid monohydrate (1.63 g, 8.55 mmol, 5.0 equiv.) was added and it was stirred at 95 °C for 1 h. The solvent was evaporated under the reduced pressure and the residue was purified by flash chromatography on silica gel (hexane-dichloromethane 20:1 to 8:1) to afford (monoF[6]H) (414 mg, 70%) as a white crystalline solid.

Optical rotation: $[\alpha]^{20}_D$ -3187° (c 0.112, $CHCl_3$); $[\alpha]^{20}_D$ +3358° (c 0.101, $CHCl_3$).

M.p.: 201-202 °C (heptane).

UV/Vis (THF): λ_{max} (log ε) = 230 (4.58), 248 (4.63), 252 (4.63), 264 (4.58), 302 (4.16), 314 (4.35), 325 (4.34), 347 nm (4.03).

^{1}H NMR (400 MHz, $CDCl_3$): 6.60 (ddd, *J* = 8.6, 7.7, 6.0, 1H), 6.74 (ddd, *J* = 8.4, 6.9, 1.4, 1H), 6.91 (ddd, *J* = 10.1, 7.8, 1.0, 1H), 7.25 (ddd, *J* = 8.0, 6.9, 1.2, 1H), 7.37 (dq, *J* = 8.6,

0.8, 1H), 7.57 (ddt, *J* = 8.5, 1.1, 0.6, 1H), 7.84 (ddd, *J* = 8.0, 1.5, 0.6, 1H), 7.93 (d, *J* = 8.6, 1H), 7.95 (d, *J* = 8.6, 1H), 7.99 (d, *J* = 8.2, 2H), 8.01 (d, *J* = 7.9, 2H), 8.03 (d, *J* = 8.2, 1H), 8.24 (dt, *J* = 8.8, 0.7, 1H).

^{19}F NMR (376 MHz, $CDCl_3$): -123.05 (dd, *J* = 10.2, 6.1)

^{13}C NMR (101 MHz, $CDCl_3$): 109.74 (d, *J* = 20.0), 119.75 (d, *J* = 7.4), 121.63 (d, *J* = 15.8), 123.74 (d, *J* = 3.8), 124.27, 124.51 (d, *J* = 8.6), 125.00, 125.78, 126.26, 126.95 (d, *J* = 1.6), 126.97, 127.34, 127.61, 127.62, 127.65, 127.67, 127.73, 128.04, 128.17, 130.03, 131.50, 131.55, 131.64 (d, *J* = 3.8), 131.88, 133.42, 158.68 (d, *J* = 248.8).

IR ($CHCl_3$): 3052 w, 1628 w, 1612 w, 1583 w, 1555 w, 1521 w, 1501 w, 1483 vw, 1470 w, 1446 m, 1436 w, 1407 m, 1392 vw, 1363 w, 1294 w, 1262 vw, 1243 m, 1174 vw, 1142 w, 1136 w, 1105 w, 1079 w, 1049 w, 1015 w, 942 w, 869 w, 854 m, 845 vs, 826 m, 627 m, 516 m cm^{-1}.

EI MS: 346 ($M^{+\bullet}$, 100), 331(23), 318 (62), 207 (15), 171 (27), 165 (28), 149 (8).

HR EI MS: calculated for $C_{26}H_{15}F$ 346.1152, found 346.1150.

HPLC Resolution of 4-fluoro[6]helicene (monoF[6]H) into enantiomers

The optimal conditions for the HPLC resolution of 4-fluoro[6]helicene (**monoF[6]H**) were found as follows: column: Chiral Art Cellulose-SB (250 x 4.6 mm ID, 5 µm, YMC), mobile phase: 20% toluene in *n*-heptane, flow rate: 1.0 ml/min, temperature: 25 °C.

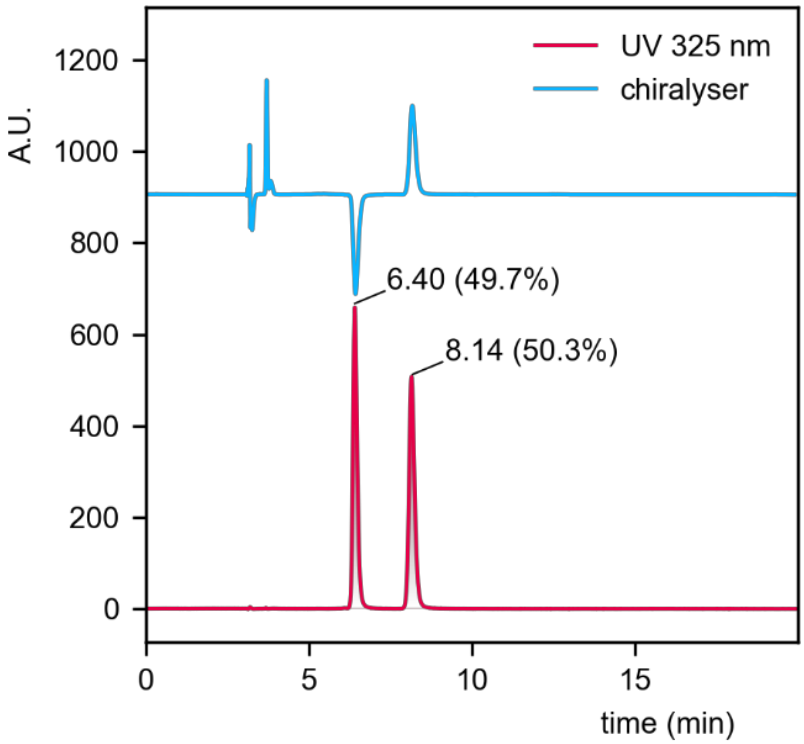

Figure S2: HPLC Resolution of 4-fluoro[6]helicene (**monoF[6]H**) into enantiomers.

On a semipreparative scale 4-fluoro[6]helicene (**monoF[6]H**) was resolved into enantiomers using the same chiral stationary phase (column: Chiral Art Cellulose-SB column, 250 x 20 mm ID, 5 µm, YMC) and a gradient of 10 to 30% of toluene in *n*-heptane over 10 min at a flow rate of 20 ml/min. Samples (cca 20 mg) were dissolved in toluene (cca 1 ml) and filtered through a PTFE membrane syringe filter (0.45 µm pore size). Both enantiomers were isolated with optical purity >99% *ee*.

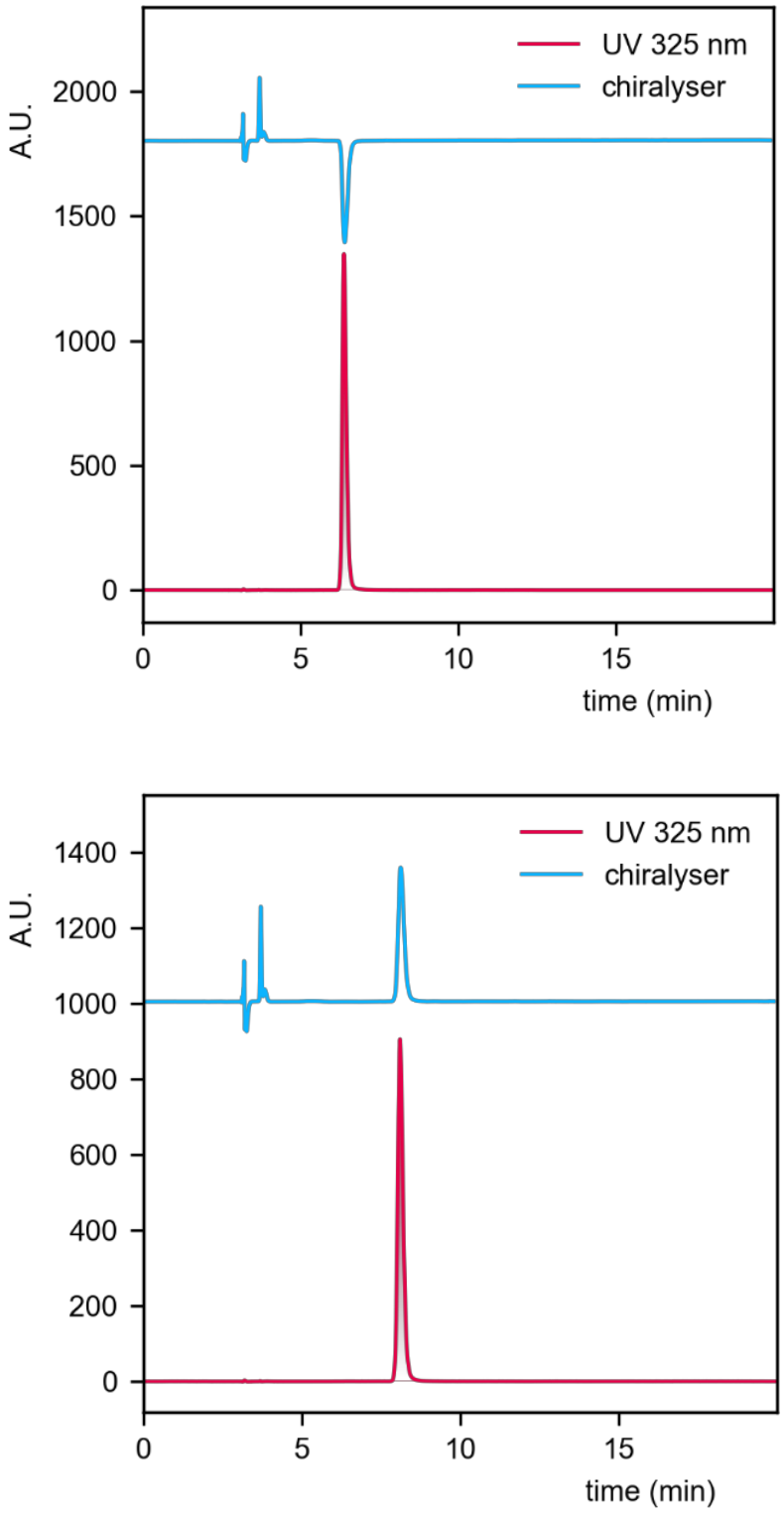

Figure S3: HPLC traces of resolved enantiomers of 4-fluoro[6]helicene (**monoF[6]H**).

Calculated *vs* experimental ECD spectra of 4-fluoro[6]helicene (monoF[6]H) enantiomers

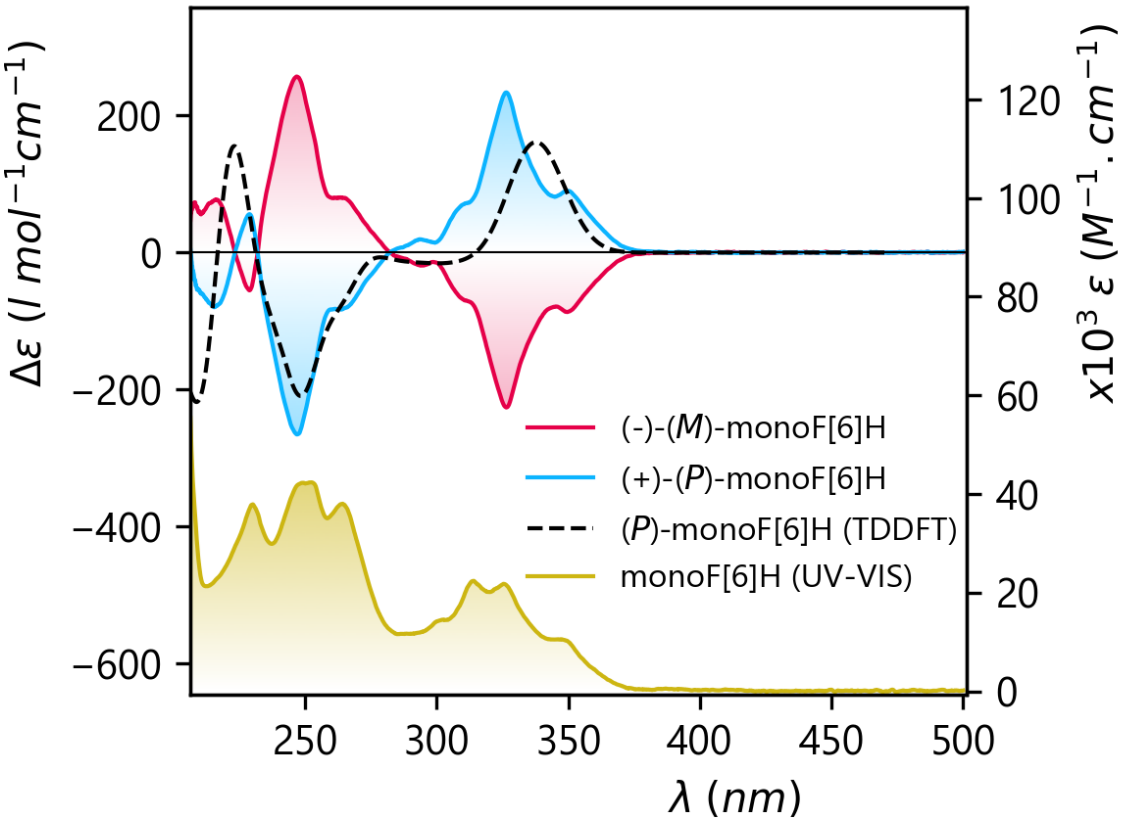

Figure S4: Calculated vs experimental ECD spectra and UV-Vis spectrum of 4-fluoro[6]helicene (**monoF[6]H**).

Absolute configuration of the resolved enantiomers of 4-fluoro[6]helicene (**monoF[6]H**) was assigned based on comparison of calculated (TD-DFT PBE0/cc-pVTZ/GD3/PCM(THF), (*P*)-enantiomer, black dashed line) and experimental (in THF, fast eluting enantiomer – red line, slow-eluting enantiomer – blue line) ECD spectra.

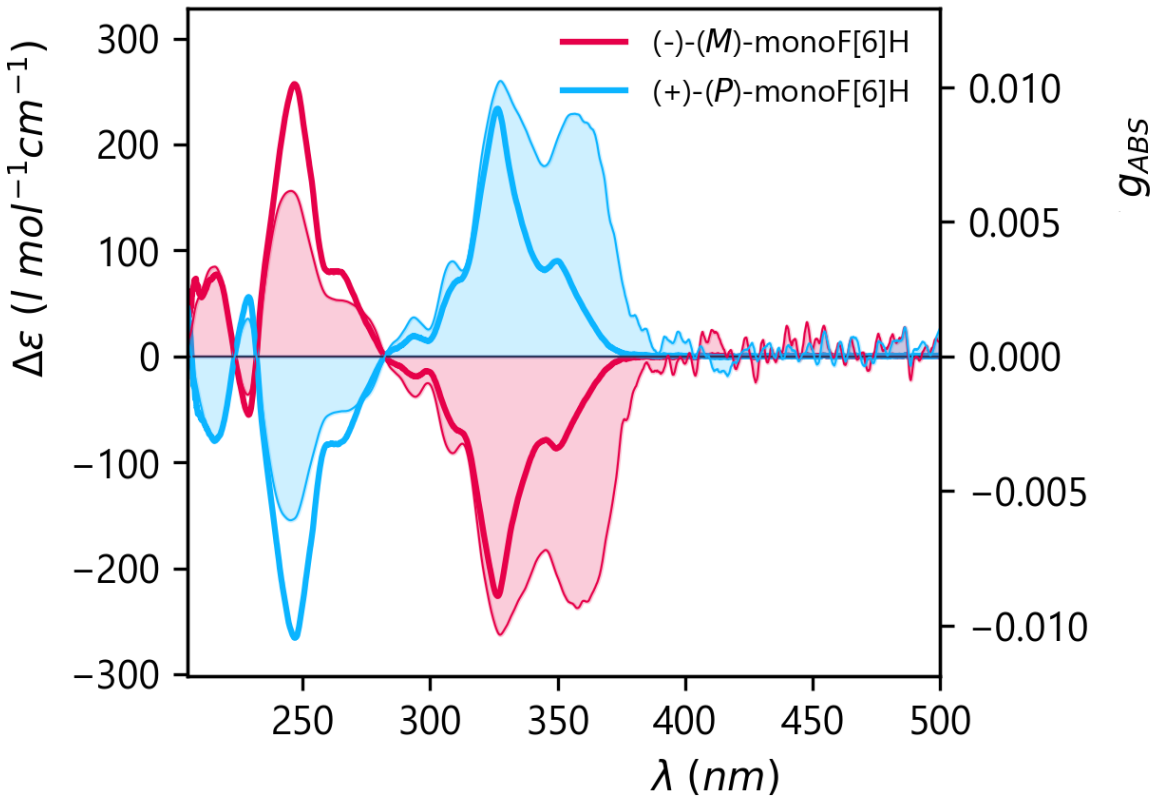

Figure S5: Experimental ECD and g_{abs} spectra of (*P*)- and (*M*)-4-fluoro[6]helicene (**monoF[6]H**).

Discussion: The maximum absorption dissymmetry factor g_{abs} was found to be 1.1 ± 10^{-2} @327 nm.

Computational details

DFT calculations were performed using Gaussian 16 software package[3]. The geometry of (*P*)-4-fluoro[6]helicene (**monoF[6]H**) was optimised by DFT at PBE0[4]/cc-pVTZ[5]/GD3[6]/PCM[7,8] (tetrahydrofuran) level of theory and subsequent vibrational analysis confirmed absence of negative vibrational frequencies.

ECD transitions were extracted from a TD-DFT calculation performed at the same level of theory for 150 lowest-energy singlet states and the CD spectrum was constructed by gaussian broadening (0.3 eV).

Cartesian coordinates for the optimised geometry and the respective TD-DFT calculated CD transitions:

HF=-1098.7961917

C	-11.098010	6.873661	-0.497245
C	-9.936219	6.066407	-0.658363
C	-9.948774	4.714063	-0.260107
C	-11.025910	4.286704	0.606327
C	-12.165655	5.120897	0.739196
C	-12.203695	6.401212	0.124074
C	-8.837173	3.879915	-0.646068
C	-7.616428	4.533056	-0.945852
C	-7.603148	5.923866	-1.218991
C	-8.751531	6.645283	-1.178745
C	-6.405668	3.797053	-0.975576
C	-6.406630	2.461211	-0.736906
C	-7.631704	1.752098	-0.663978
C	-8.857754	2.442085	-0.754703
C	-10.037497	1.661717	-1.059847
C	-9.988852	0.249516	-0.932768
C	-8.757577	-0.389217	-0.615924
C	-7.614841	0.332556	-0.548162
C	-11.142497	-0.516791	-1.189261
C	-12.299984	0.073211	-1.626740
C	-12.324769	1.456726	-1.849222
C	-11.223303	2.226270	-1.570390
H	-11.076540	7.884343	-0.888418
H	-13.093001	7.008805	0.222642
H	-6.664047	6.386650	-1.499552
H	-8.763760	7.690655	-1.464233
H	-5.479581	4.331151	-1.154197
H	-5.478434	1.904540	-0.679830
H	-8.742366	-1.467062	-0.501469
H	-6.658511	-0.157031	-0.403205
H	-11.087754	-1.592101	-1.060529
H	-13.178631	-0.526949	-1.829608
H	-13.216114	1.924397	-2.249621
H	-11.263505	3.287770	-1.767032
C	-13.219477	4.678638	1.556363
C	-13.173899	3.522275	2.278559

C	-12.005491	2.752545	2.209850
C	-10.964269	3.122186	1.397159
H	-14.010675	3.240370	2.903763
H	-11.925040	1.855880	2.811395
H	-10.072226	2.514615	1.379709
F	-14.307563	5.462022	1.645805

[Wavelength (nm), R(length)], [371.566, -1.290], [356.307, -1.582], [336.575, 691.69], [321.585, -138.4], [312.294, 50.754], [304.711, -57.04], [291.288, -17.58], [287.893, 0.2668], [282.855, -8.928], [279.224, -18.65], [270.554, 68.284], [264.759, -168.8], [258.381, -58.45], [248.430, -385.7], [245.717, -38.92], [238.486, 85.547], [237.722, -182.1], [232.729, -36.67], [228.824, 20.561], [224.279, 87.567], [222.321, 173.78], [221.356, 28.826], [218.385, -6.845], [217.283, 11.099], [211.580, -71.60], [210.853, -227.6], [208.987, 31.787], [206.385, -60.51], [204.969, -6.284], [203.814, -130.7], [200.992, -2.690], [200.624, 33.185], [199.955, -5.215], [198.476, -10.74], [197.887, -18.67], [196.432, -19.91], [195.620, -2.017], [195.229, -2.105], [194.077, 0.8546], [191.558, 78.653], [191.174, 62.741], [190.294, 45.976], [189.210, 17.549], [188.088, 60.206], [185.555, 52.205], [185.505, 58.525], [183.313, -7.316], [182.886, 17.621], [182.442, 48.673], [181.488, 133.91], [181.231, 85.499], [180.474, 3.1263], [179.924, -7.617], [179.344, -2.324], [178.811, -12.77], [178.409, 4.2122], [178.046, -37.46], [177.219, -0.891], [177.029, -20.49], [176.834, -81.30], [176.266, -1.846], [175.565, -5.576], [174.943, 2.9675], [174.198, -9.569], [173.966, 3.4206], [173.142, -2.587], [172.427, 2.3335], [172.300, 9.9869], [171.483, -1.065], [170.293, -3.018], [168.764, -25.90], [168.527, -22.57], [167.779, -7.375], [167.625, -14.86], [167.011, 10.062], [166.964, -6.562], [166.710, -4.425], [166.580, -6.144], [166.544, 7.1605], [166.107, -0.025], [165.716, -118.3], [164.714, 6.1235], [164.598, 19.493], [163.496, -0.822], [163.429, -4.599], [163.298, -11.06], [163.119, -2.848], [162.340, -2.458], [162.161, 0.3635], [161.250, -25.89], [160.957, -3.448], [160.688, 8.0542], [160.547, 2.6920], [160.335, -0.921], [159.878, -2.853], [159.479, 2.8844], [159.201, 2.1980], [158.970, -5.519], [158.732, -28.93], [158.294, -10.08], [157.688, -11.08], [157.284, -5.549], [157.230, 3.5810], [156.834, 7.1219], [156.616, -5.548], [156.362, -7.647], [156.194, -5.464], [155.495, -35.37], [155.224, -2.481], [155.096, -0.319], [154.813, -0.299], [154.107, -10.73], [153.845, -9.148], [153.674, -1.839], [153.400, -12.92], [152.748, 5.1142], [152.412, -2.866], [152.238, 14.200], [151.813, 3.4516], [151.316, -7.067], [151.078, -5.168], [150.511, -18.63], [150.433, -2.825], [150.169, -3.793], [149.880, -6.281], [149.668, 8.9839], [149.378, 9.8888], [149.044, 2.4268], [148.754, -8.976], [148.400, 14.243], [148.212, 3.6914], [148.009, 10.659], [147.887, 8.3804], [147.601, 23.311], [147.412, 7.2801], [147.165, 14.306], [146.928, 18.213], [146.752, 27.403], [146.596, -4.779], [146.527, 6.7908], [145.814, 1.3970], [145.596, -7.014], [145.206, -1.006], [145.049, -5.172], [144.778, -1.512], [144.748, 7.2800], [144.399, -12.04], [144.097, 9.5810], [144.067, 10.948], [143.950, -9.813].

NMR spectra of compounds (3) to (monoF[6]H)

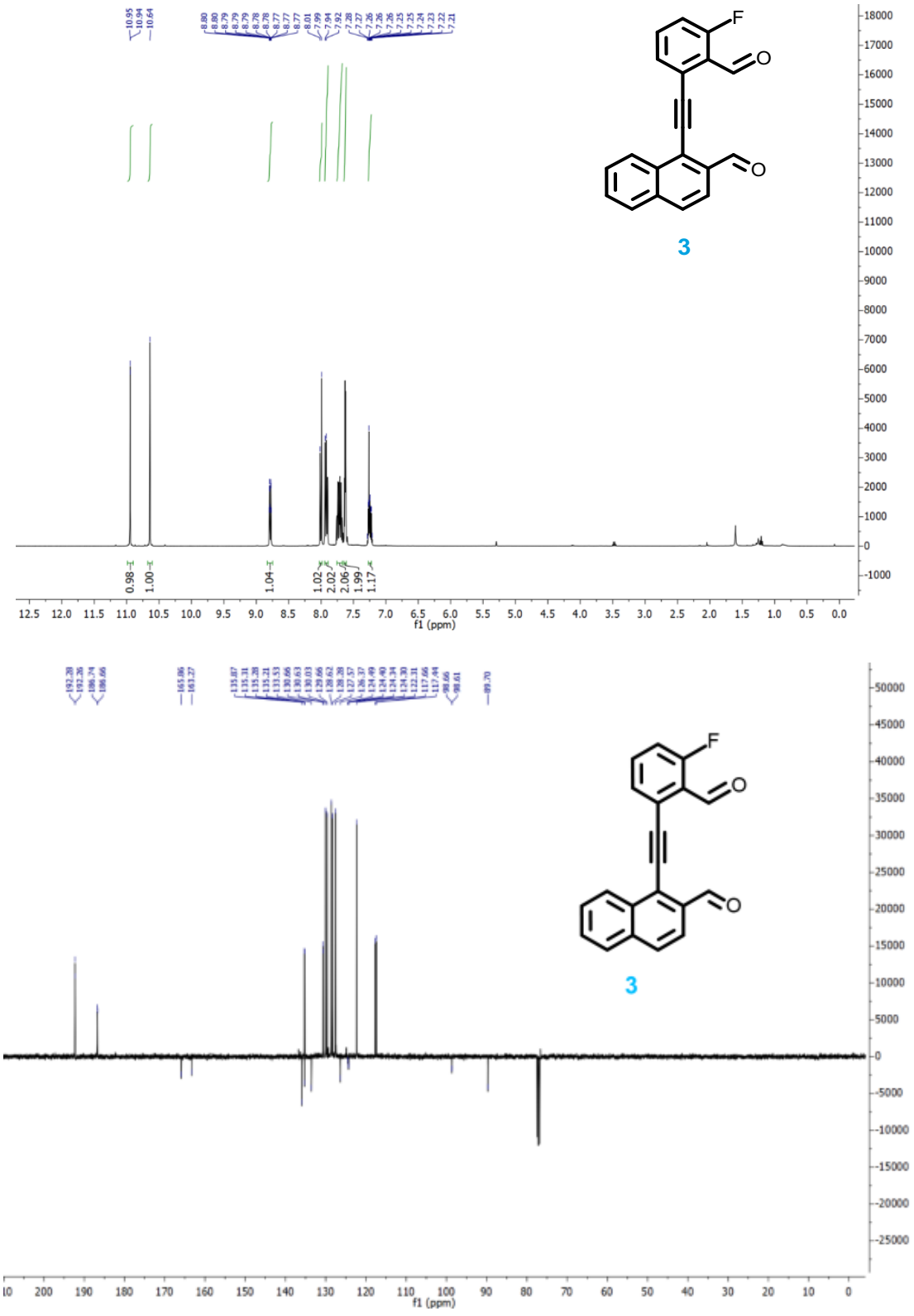

Figure S6: ^{1}H and ^{13}C NMR spectra of compound 3.

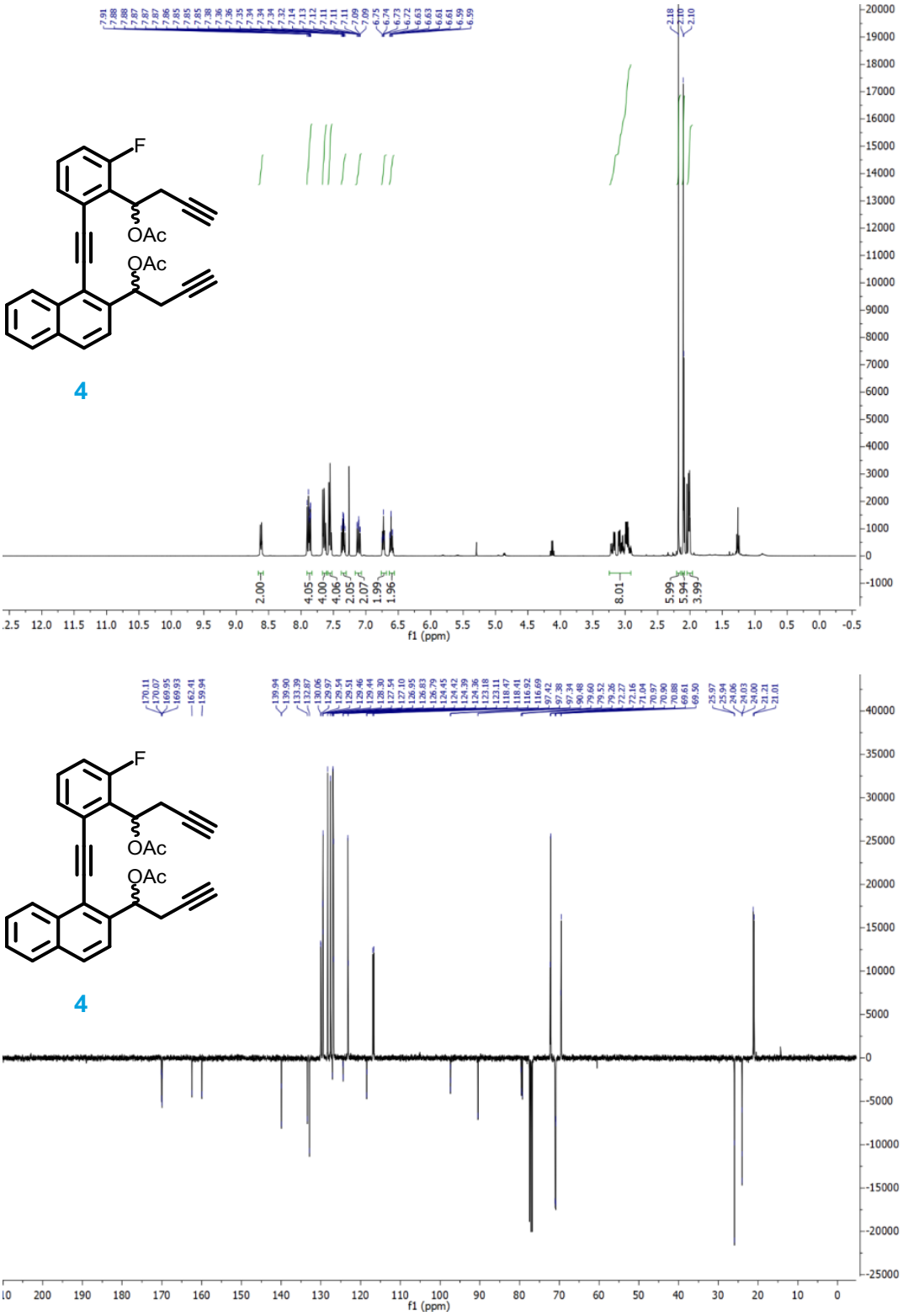

Figure S7: ^{1}H and ^{13}C spectra of compound **4**.

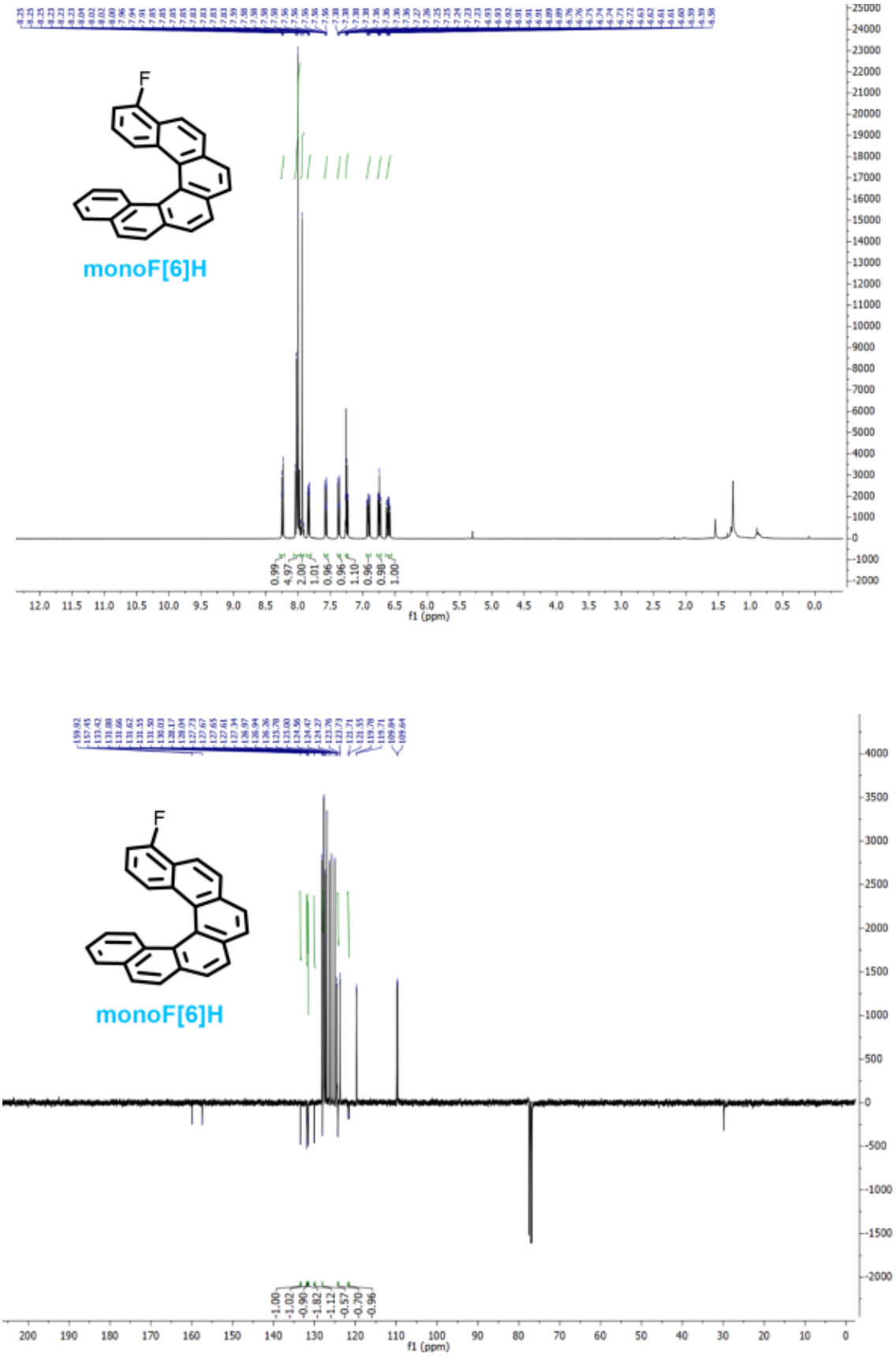

Figure S8: ^{1}H and ^{13}C spectra of compound (**monoF[6]H**).

Optical and chiroptical analysis of F8BT:Chiral additive thin films

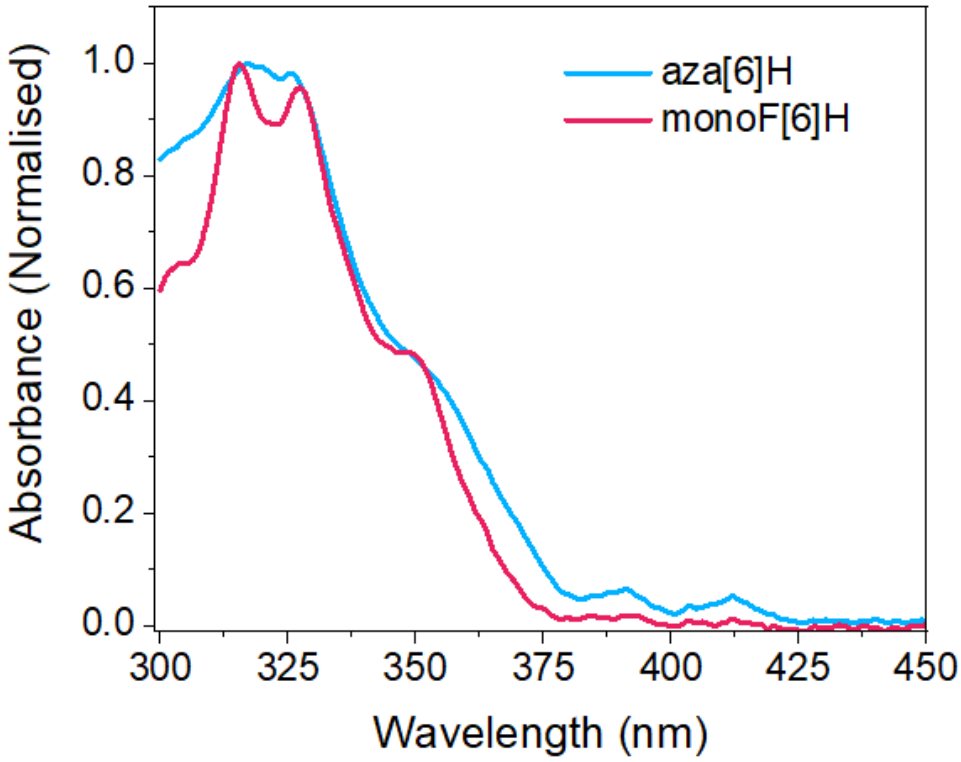

Figure S9: Optical absorption of chiral additives, measured in toluene with a concentration of 10^{-5} M.

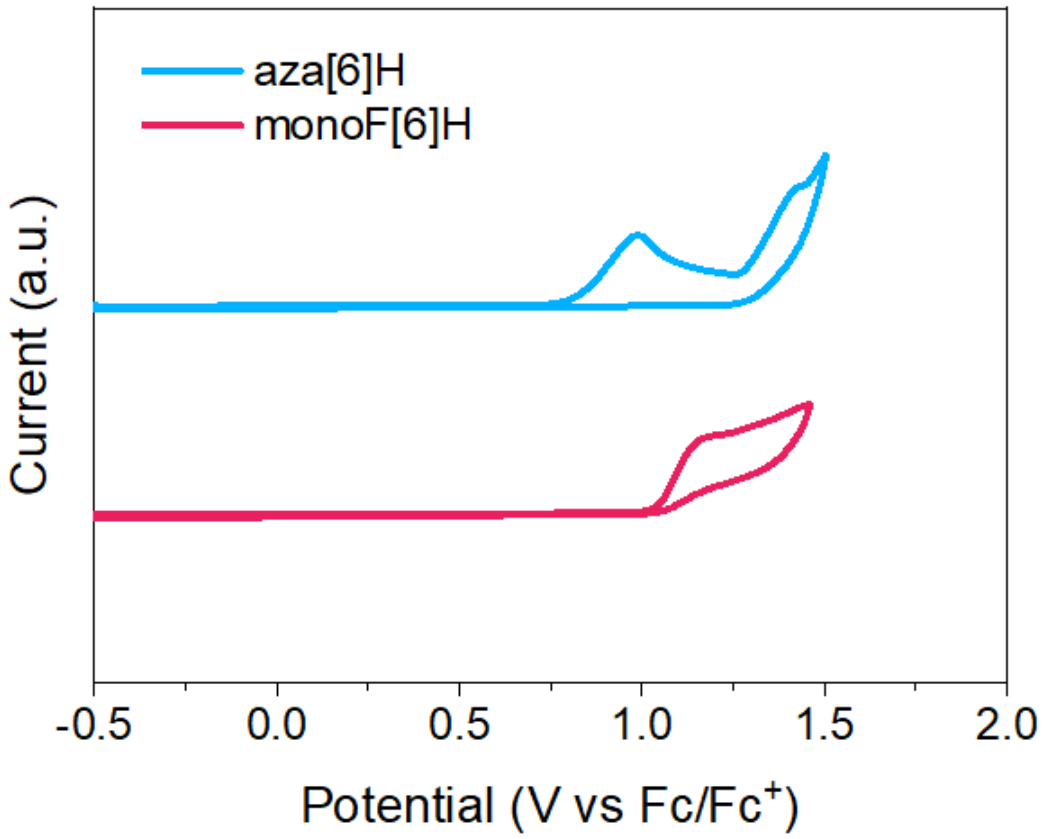

Figure S10: Cyclic voltammetry (oxidation) of aza[6]H and monoF[6]H.

	HOMO, from CV	**Energy gap (eV), optical**	**Estimated LUMO (HOMO CV + E_g)**
aza[6]H	5.6	3.22	2.38
monoF[6]H	5.8	3.30	2.5

Table S1: Estimation of energy levels of aza[6]H and monoF[6]H.

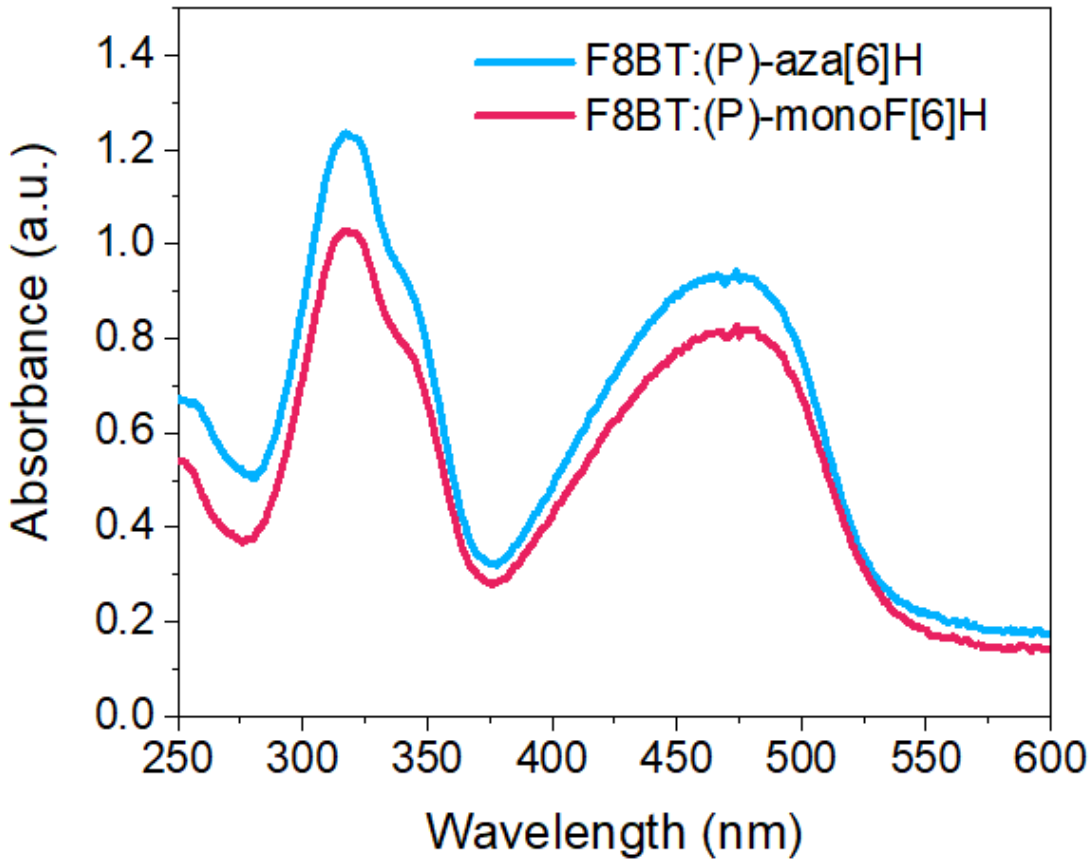

Figure S11: Absorption of F8BT:(P)-aza[6]H and F8BT:(P)-monoF[6]H thin films, annealed at 140°C.

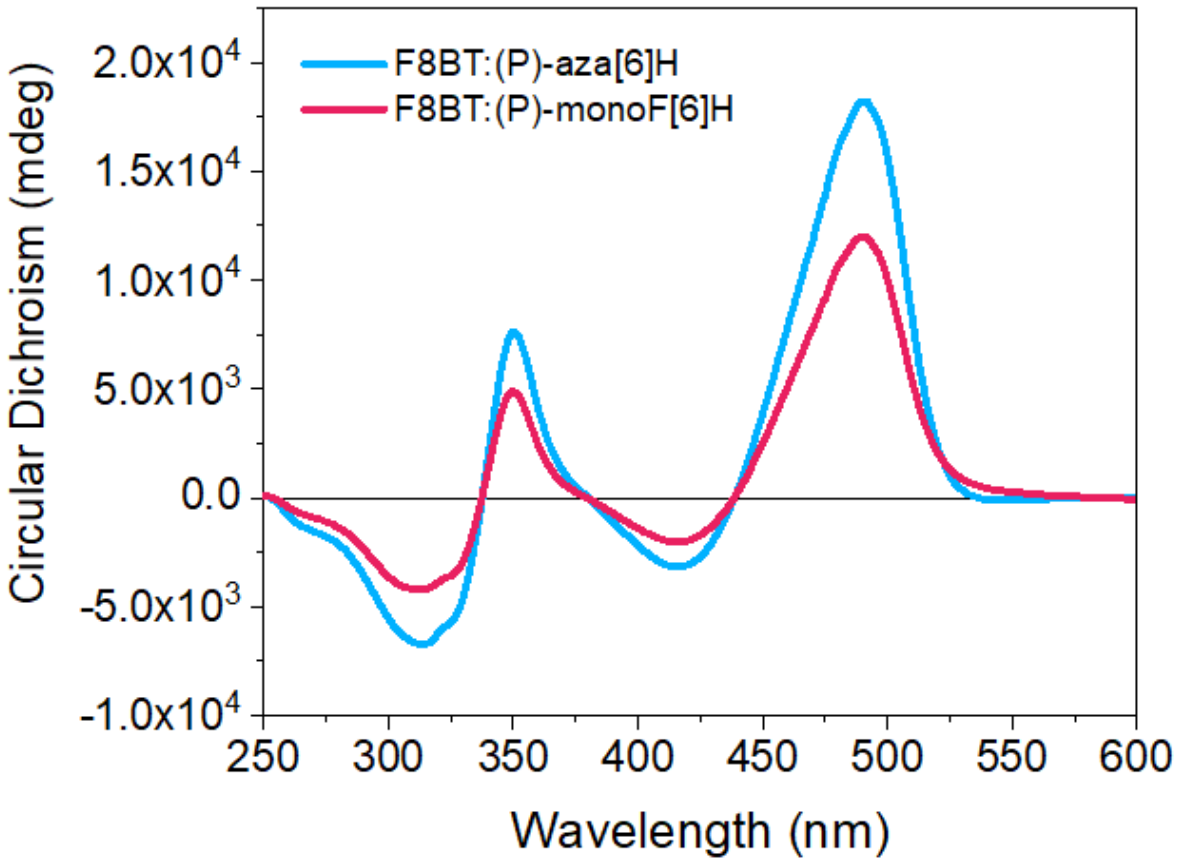

Figure S12: Circular dichroism of annealed thin films (140 °C) of F8BT:(*P*)-aza[6]H and F8BT:(*P*)-monoF[6]H, with a thickness of 160 nm.

Dissimmetry factor g_{abs} is calculated from these spectra.

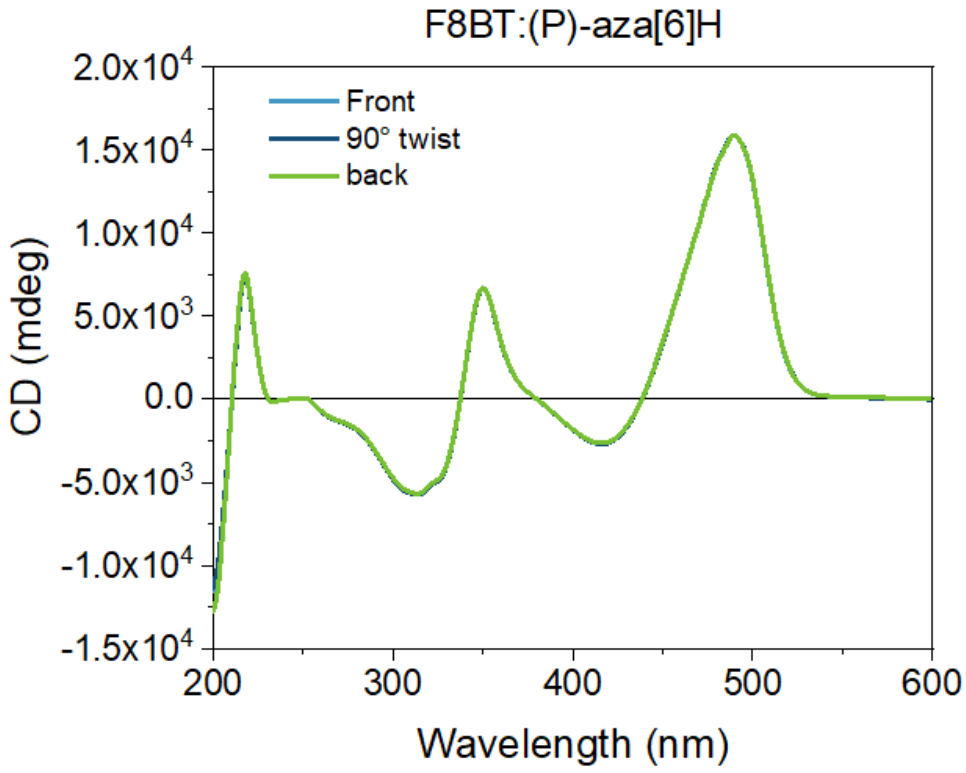

Figure S13: CD spectra of F8BT:(*P*)-aza[6]H, measured with front, 90° twisted and back excitation.

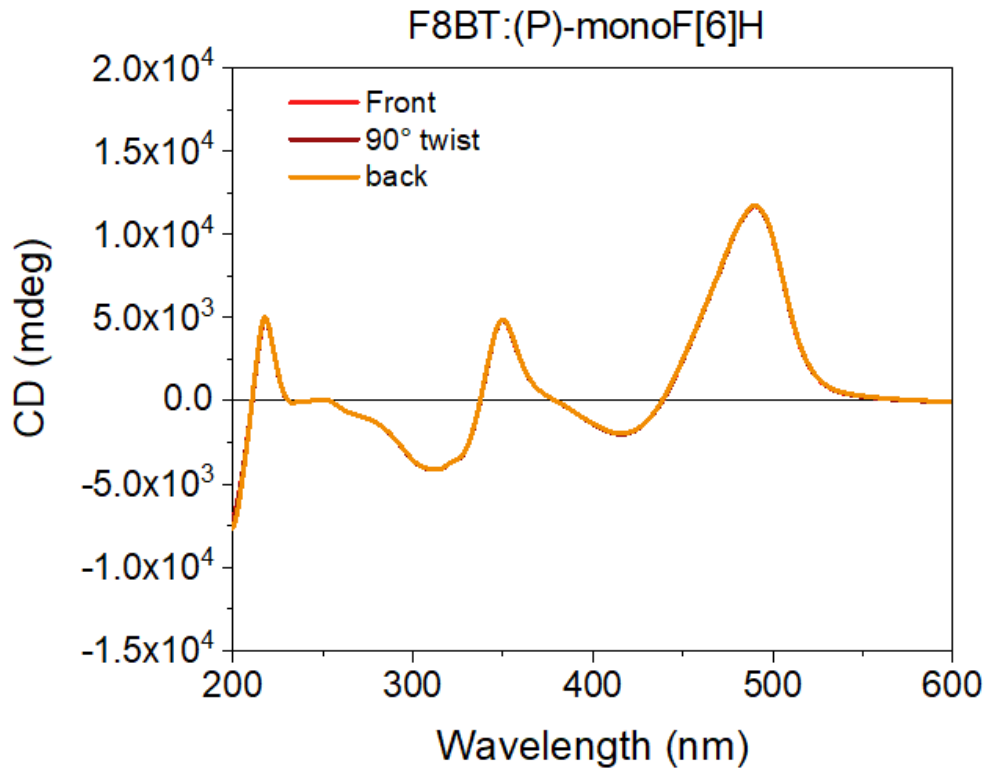

Figure S14: CD spectra of F8BT:(*P*)-monoF[6]H, measured with front, 90° twisted and back excitation.

Muller Matrix Ellipsometry Analysis

Muller matrix analysis is a technique to describe the behaviour of optically active materials upon interaction with CP light. Specifically, probing the sample optically allows the analysis of the transformation between the initial state of polarisation of the light and the final state after it is transmitted or reflected by the material. The transformation of the incident light by the active material can be described by a 4x4 matrix, with each element representing different optical properties of the sample (LD: Linear Dichroism, LB: Linear Birefringence; CD: Circular Dichroism; CB: Circular Birefringence, T: Transmittance):

$$MM = \begin{pmatrix} m_{00} & m_{01} & m_{02} & m_{03} \\ m_{10} & m_{11} & m_{12} & m_{13} \\ m_{20} & m_{21} & m_{22} & m_{23} \\ m_{30} & m_{31} & m_{32} & m_{33} \end{pmatrix} = \begin{pmatrix} T & -LD & -LD' & CD \\ -LD & T & CB & -LB' \\ -LD & -CB & T & -LB \\ CD & -LB' & LB & T \end{pmatrix}$$

In this case, MM analysis was carried out in transmittance mode at Diamond Light Source using B23 beamline Mueller Matrix Polarimeter (MMP)[9]. The results of figures S12 and S13 indicated that LD and LB were negligible and that the CD elements m_{30} and m_{03} were symmetric, whilst CB elements m_{21} and m_{12} were anti-symmetric as they would be if no depolarisation was occurring.

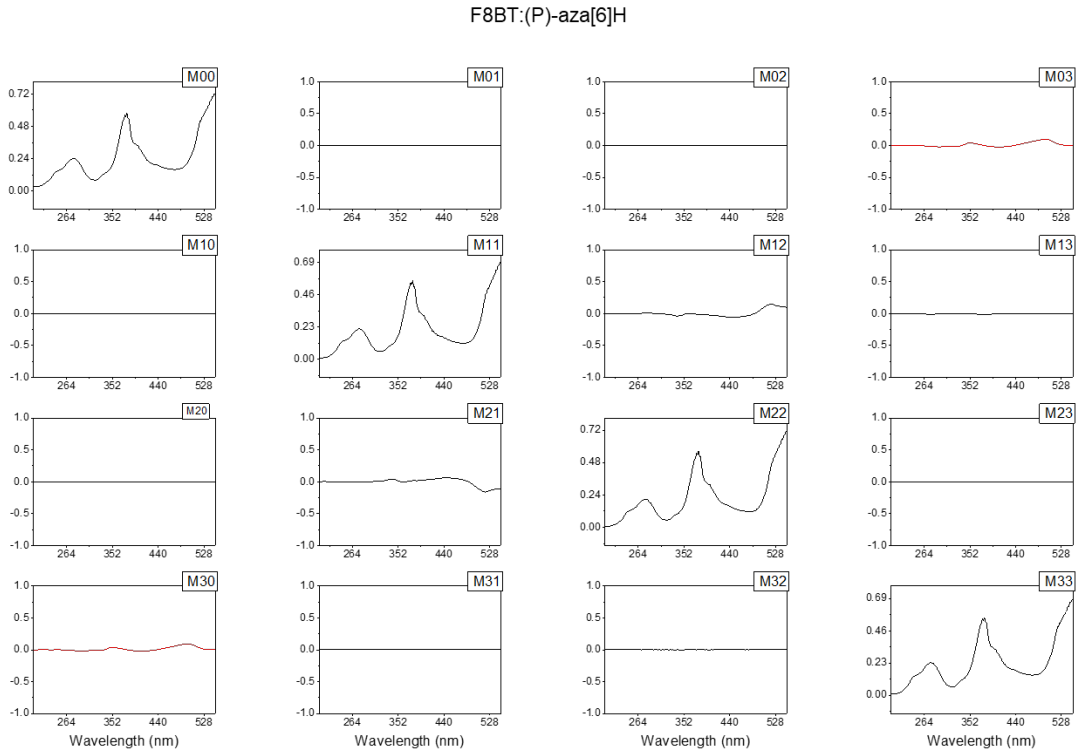

Figure S15: Differential Muller Matrix of thermally annealed thin film F8BT:(*P*)-aza[6]H blends. CD components are highlighted in red.

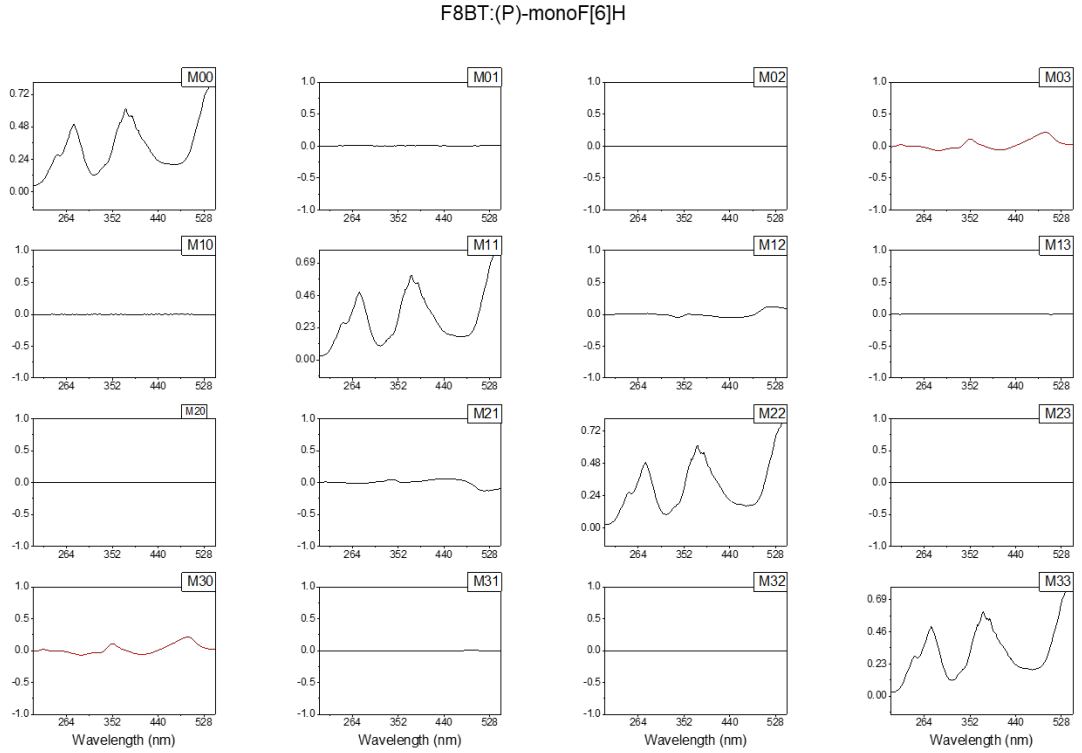

Figure S16: Differential Muller Matrix of thermally annealed thin film F8BT:(*P*)-monoF[6]H blends. CD components are highlighted in red.

Circularly Polarised Photoluminescence

All CPPL measurements are carried out with a 180° excitation geometry

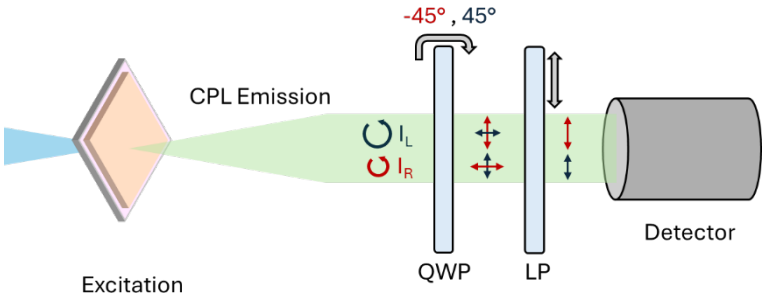

Scheme S17: Excitation and detection geometry of recorded CPL

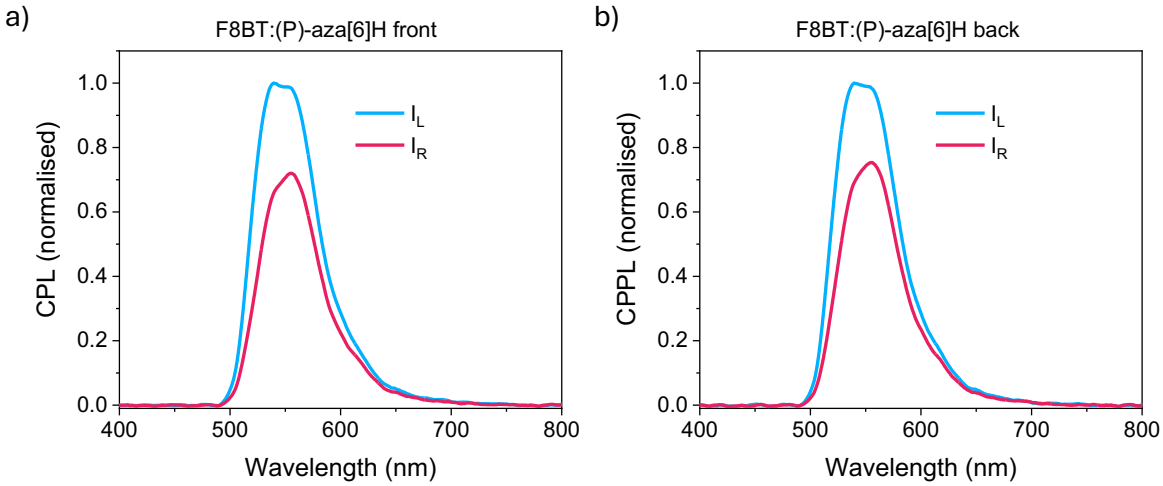

Figure S18: Circularly polarised photoluminescence of annealed F8BT:(*P*)-aza[6]H thin film, with a) front side and b) back-side excitation.

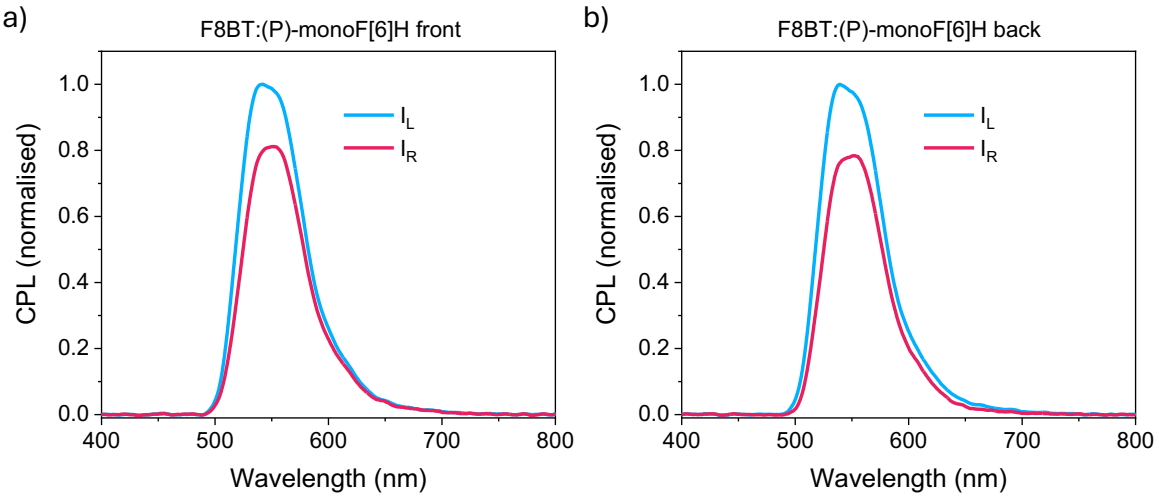

Figure S19: Circularly polarised photoluminescence of film F8BT:(*P*)-monoF[6]H thin film, with a) front side and b) back-side excitation.

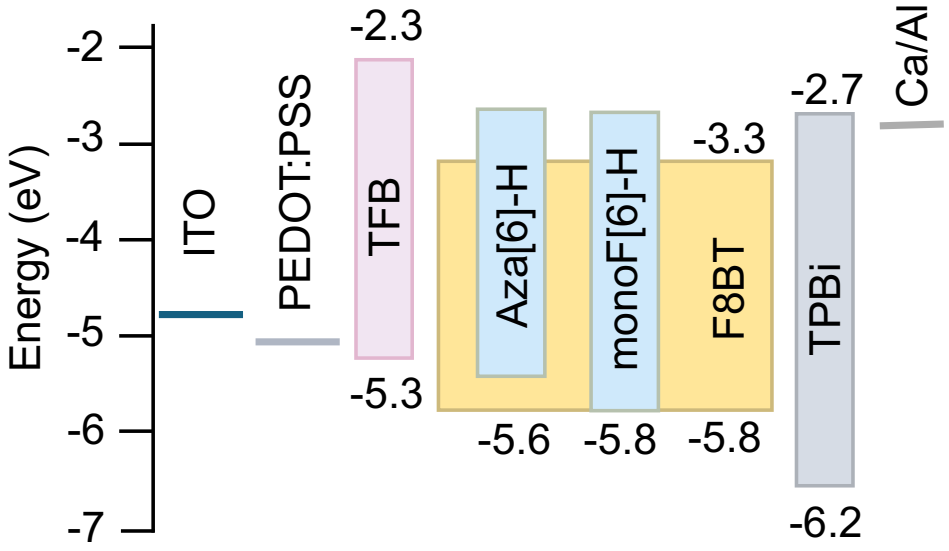

Figure S20: Energy diagram of conventional CP-OLEDs.

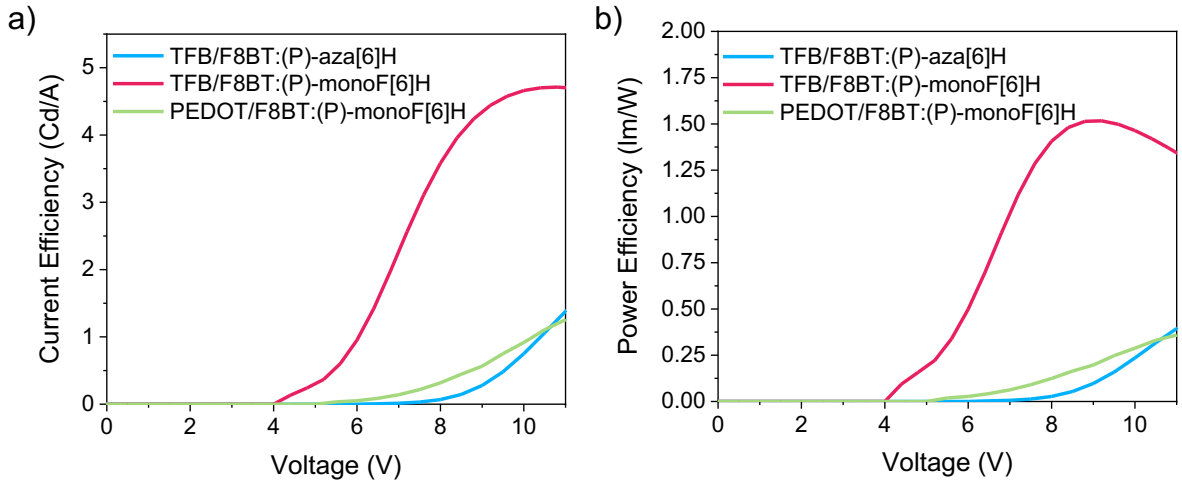

Figure S21: Current efficiency and power efficiency of conventional CP-OLEDs, based on different combinations of HTL/F8BT:chiral additive.

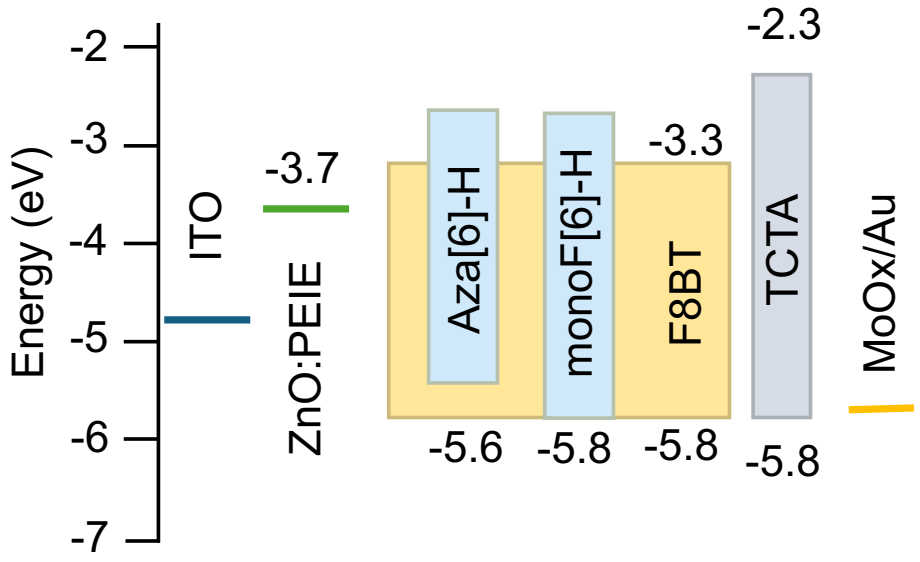

Figure S22: Energy diagram of inverted CP-OLEDs.

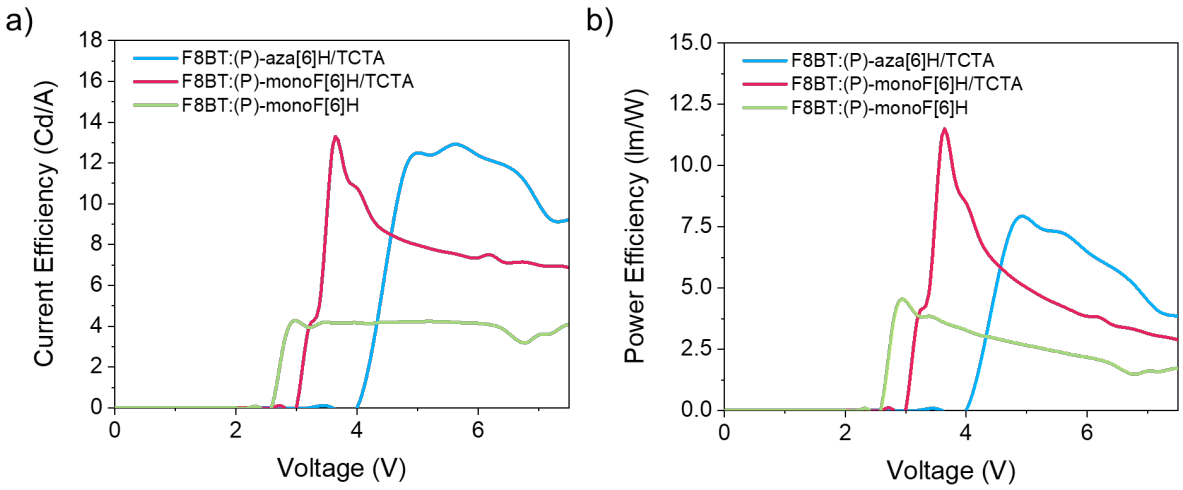

Figure S23: Current efficiency and power efficiency of inverted CP-OLEDs.

Device Structure	Turn on Voltage (V_{ON}, V)	Maximum Luminance (L_{max}, Cd/m^2)	Current Efficiency (Cd/A)	External Quantum Efficiency (%)	Power Efficiency (lm/W)
Conventional Structure					
ITO/PEDOT:PSS/F8BT:(*P*)-monoF[6]H/TPBi(10nm)/Ca/Al	6.5	3015	1.25	0.31	0.35
ITO/PEDOT:PSS/TFB/F8BT:(*P*)-monoF[6]H/TPBi(10nm)/Ca/Al	5.6	948	4.7	1.10	1.51
ITO/PEDOT:PSS/TFB/F8BT:(*P*)-aza[6]H/TPBi(10nm)/Ca/Al	7.5	637	1.38	0.4	0.39
Inverted Structure					
ITO/ZnO:PEIE/F8BT:(*P*)-monoF[6]H/MoOx/Au	2.7	26152	4.3	1.2	4.47
ITO/ZnO:PEIE/F8BT:(*P*)-monoF[6]H/TCTA(10nm)/MoOx/Au	3.5	7429	12.9	3.4	11.2
ITO/ZnO:PEIE/F8BT:(*P*)-aza[6]H/TCTA(10nm)/MoOx/Au	4.3	13284	12.9	3.4	7.7

Table S2: Summary of CP-OLEDs performances, with conventional and inverted structure.

Space-charge-limited current analysis

J-V curves of single-carrier only diodes were fitted with the Mott-Gurney equation, modified for the field-dependent mobility:

$$J = \frac{9}{8}\varepsilon\varepsilon_0\mu_0\frac{(V - V_{bi})}{L^3}exp\left(0.89\gamma\sqrt{\frac{(V - V_{bi})}{L}}\right)\frac{qN_tL^2}{2\varepsilon\varepsilon_0}$$

Where ε is the relative dielectric constant of the material (3 was assumed), ε_0 the vacuum permittivity, μ_0 the zero-field mobility, V_{bi} the built-in potential resulting from the work function difference of the electrodes, L the film thickness, γ is the field activation factor of mobility, and V is the applied voltage corrected for the voltage drop across the series resistance due to contacts. Extracting the values of μ_0 and γ from the experimental data, the value of μ at any field E can be obtained by using the Poole–Frenkel expression:

$$\mu = \mu_0 exp\left(\gamma\sqrt{E}\right)$$

The trap density can be extracted from the plot of the J-V curve on a log–log scale in the so-called trap-filled-limit voltage:

$$V_{TFL} = \frac{qN_tL^2}{2\varepsilon\varepsilon_0}$$

With q the elementary charge and N_t the trap density. The voltage V_{TFL} is the chosen crossing point between the tangent of the Ohmic Regime (slope $n = 1$) and the tangent of the trap-limited SCLC regime (slope $n > 1$).

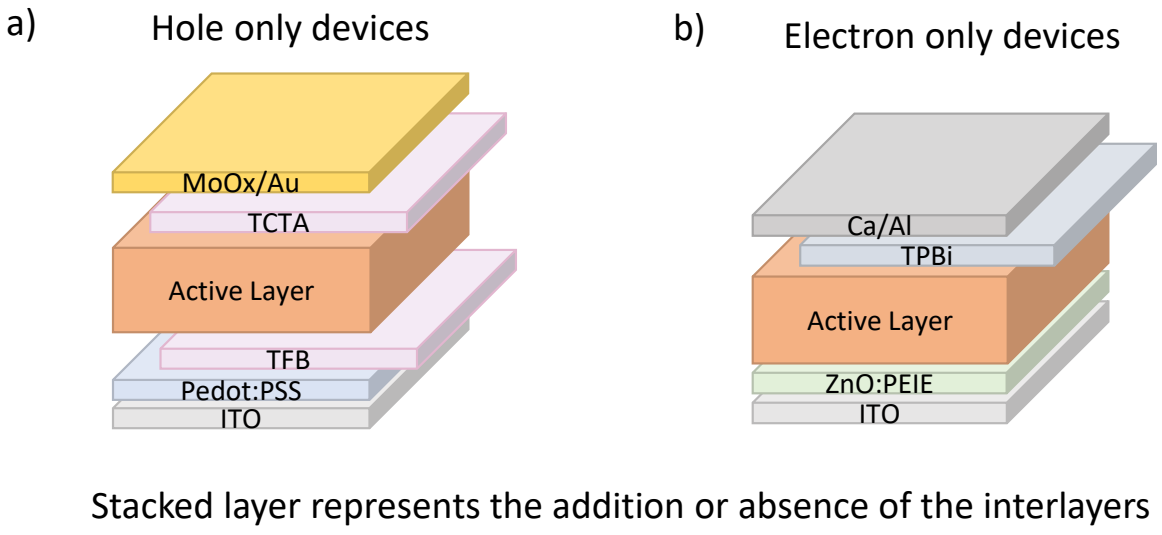

Figure S24: Device structure of a) hole only and b) electron only diodes, employed for SCLC measurements.

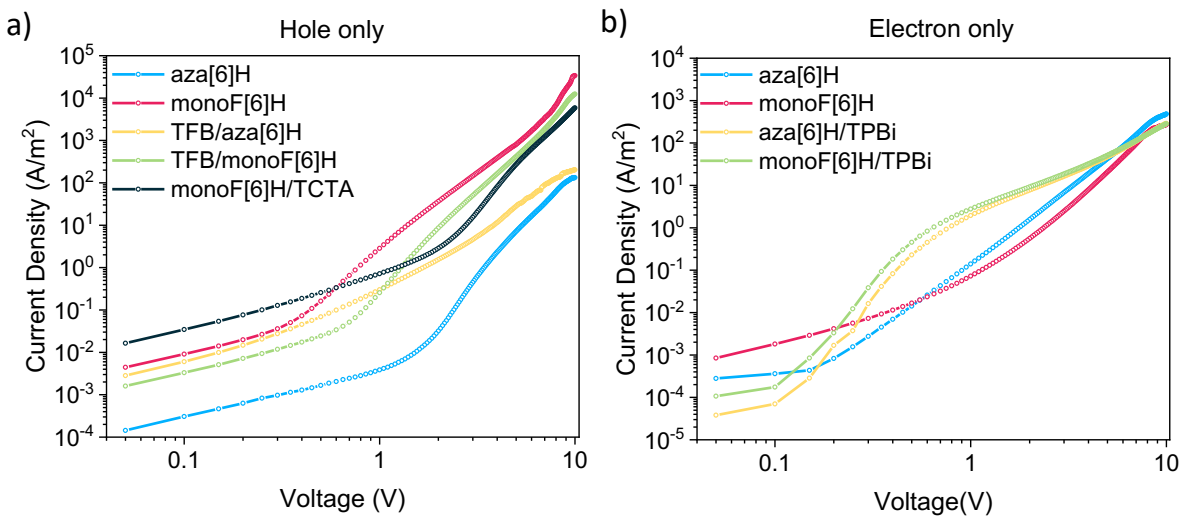

Figure S25: J-V curves and SLCL fitting of a) hole only diodes and b) electron only diodes.

Organic semiconductor stack	**Hole Mobility ($cm^2/V\ s$)**	**Hole Trap Density (cm^{-3})**	**Electron Mobility (cm^{-3})**	**Electron Trap Density (cm^{-3})**
F8BT:aza[6]H	5.2×10^{-9}	2.3×10^{16}	1.8×10^{-6}	2.5×10^{15}
F8BT:monoF[6]H	4.3×10^{-6}	4.4×10^{15}	2.1×10^{-6}	3.8×10^{15}
TFB/F8BT:aza[6]H	4.9×10^{-7}	2×10^{16}	//	//
TFB/F8BT:monoF[6]H	8.8×10^{-7}	8.2×10^{15}	//	//
F8BT:monoF[6]H/TCTA	1.8×10^{-7}	1.8×10^{16}	//	//
F8BT:aza[6]H/TPBi	//	//	2.9×10^{-6}	1.9×10^{15}
F8BT:monoF[6]H/TPBi	//	//	2.2×10^{-6}	1.7×10^{15}

Table S3: Mobilities and effective mobilities for different active layers, with or without different HTL.

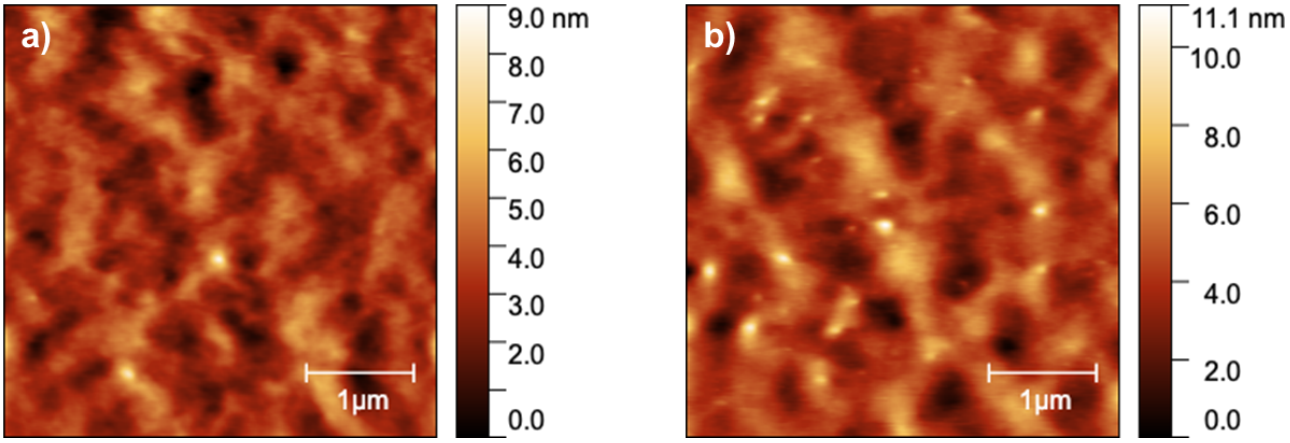

Figure S26: AFM of F8BT:chiral additive thin films, annealed at 140°C. a) F8BT:(P)-aza[6]H b)F8BT:(P)-monoF[6]H

Electrical analysis and stability

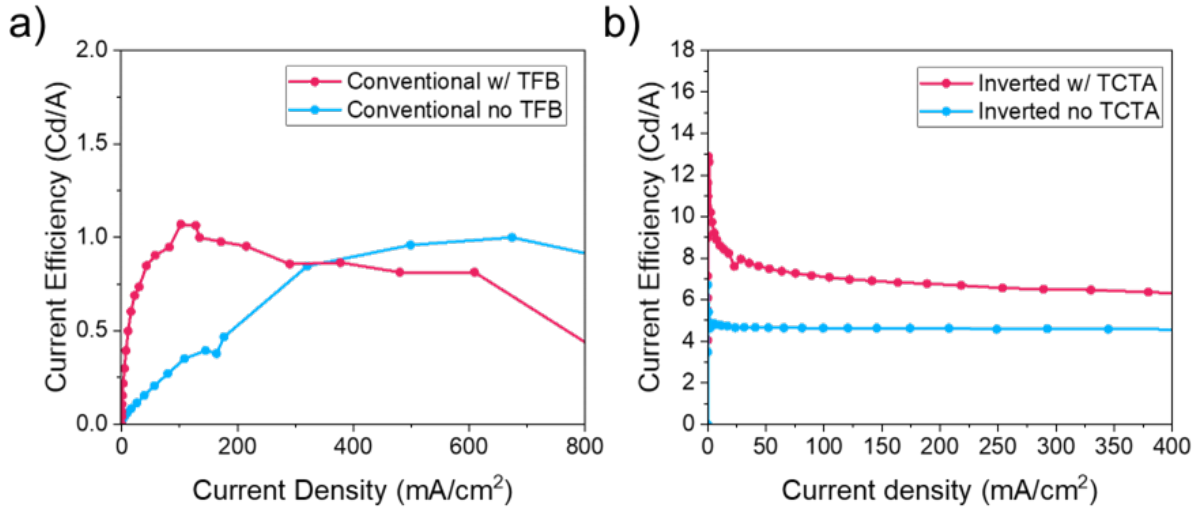

Figure S27: Current efficiency roll-off of (a) conventional and (b) inverted CP-OLEDs, with and without HTL

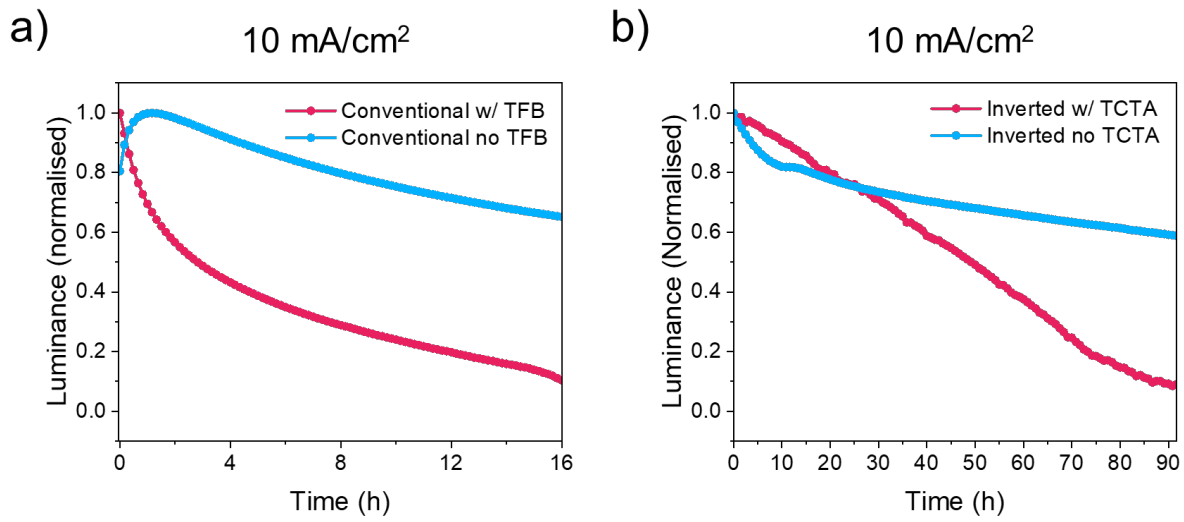

Figure S28: Stability of (a) conventional and (b) inverted CP-OLEDs, with and without HTL, measured at 10 mA/cm²

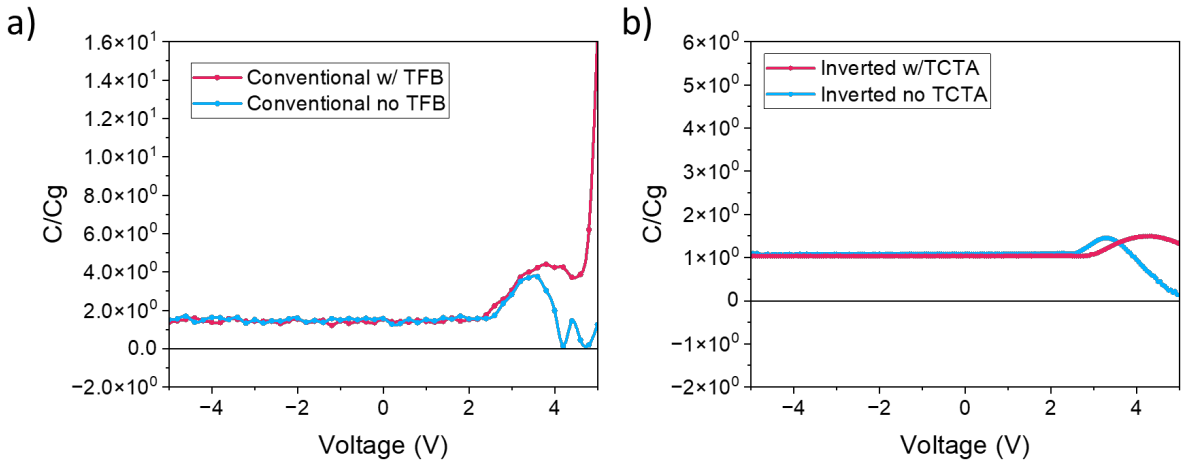

Figure S29: Capacitance voltage measurements (*f*=1kHz) for a) conventional devices with or without TFB as HTL b) Inverted devices with or without TCTA as HTL

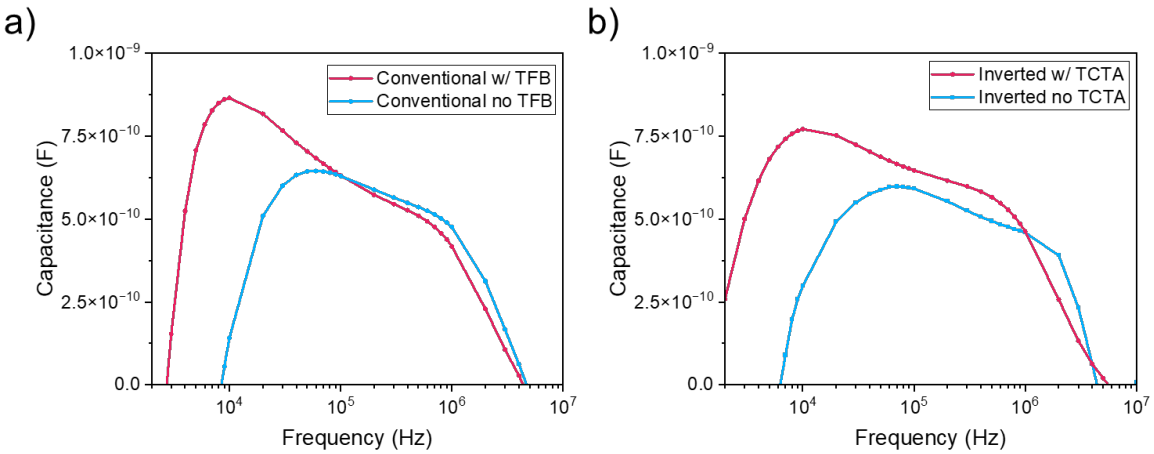

Figure S30: Capacitance frequency measurements for a) conventional devices with or without TFB as HTL b) Inverted devices with or without TCTA as HTL

Summary of CP-OLEDs emission characteristics

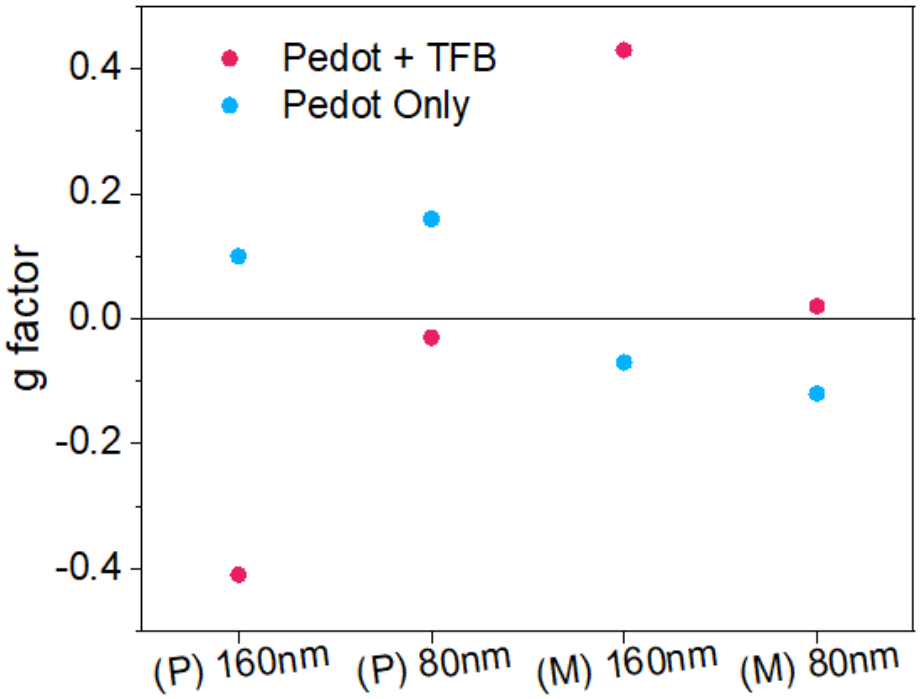

Figure S31: g-factor extracted from CP-EL for conventional CP-OLEDs based on F8BT:(*P*/*M*)-monoF[6]H and F8BT:(*M*)-monoF[6]H, thick (160 nm) and thin (80 nm) films.

Device configuration	Electron Mobility ($cm^2/V s$)	Hole Mobility ($cm^2/V s$)	Comments
Conventional: ITO/PEDOT:PSS/ /F8BT:monoF[6]H/ /TPBi/Ca/Al	2.2 x 10^{-6}	4.3 x 10^{-6}	Balanced hole and electron transport, RZ in the middle of the device. Preferential *LH* CP light emission
Conventional: ITO/PEDOT:PSS/TFB /F8BT:monoF[6]H/ /TPBi/Ca/Al	2.2 x 10^{-6}	8.8 x 10^{-7}	Unbalanced hole and electron transport, RZ close to ITO. Preferential *RH* CP light emission
Inverted: ITO/ZnO:PEIE/ /F8BT:monoF[6]H/ /MoOx/Au	2.1 x 10^{-6}	1.1 x 10^{-6}	Balanced hole and electron transport, RZ in the middle of the device. Preferential *LH* CP light emission
Inverted: ITO/ZnO:PEIE/ /F8BT:monoF[6]H/ /TCTA/MoOx/Au	2.1 x 10^{-6}	1.8 x 10^{-7}	Unbalanced hole and electron transport, RZ close to Au. Preferential L*H* CP light emission, inverted compared to conventional devices

Table S4: Summary of device mobility characteristics and CP-EL emission for F8BT:(*P*)-monoF[6]H CP-OLEDs.

Table note: While TCTA can ensure an ohmic contact with F8BT, the HOMO of TFB is shallower (5.3 eV), meaning that even if the difference between hole and electron mobilities is not as extreme as in the case of TFB-based devices. Moreover, for thin TFB films (like in these devices), Ohmic losses can also occur at the interface with PEDOT:PSS[10]. Therefore, recombination will still be pinned close to the TFB interface because of non-ohmic injection from TFB.

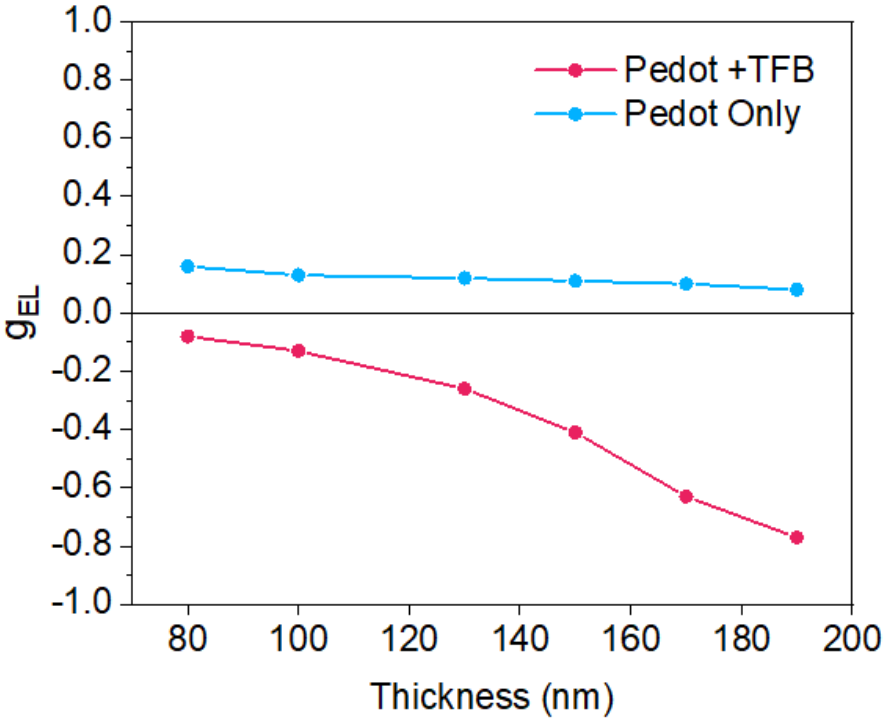

Figure S32: CP-EL as a function of thickness for conventional CP-OLEDs based on F8BT:(*P*)-monoF[6]H.

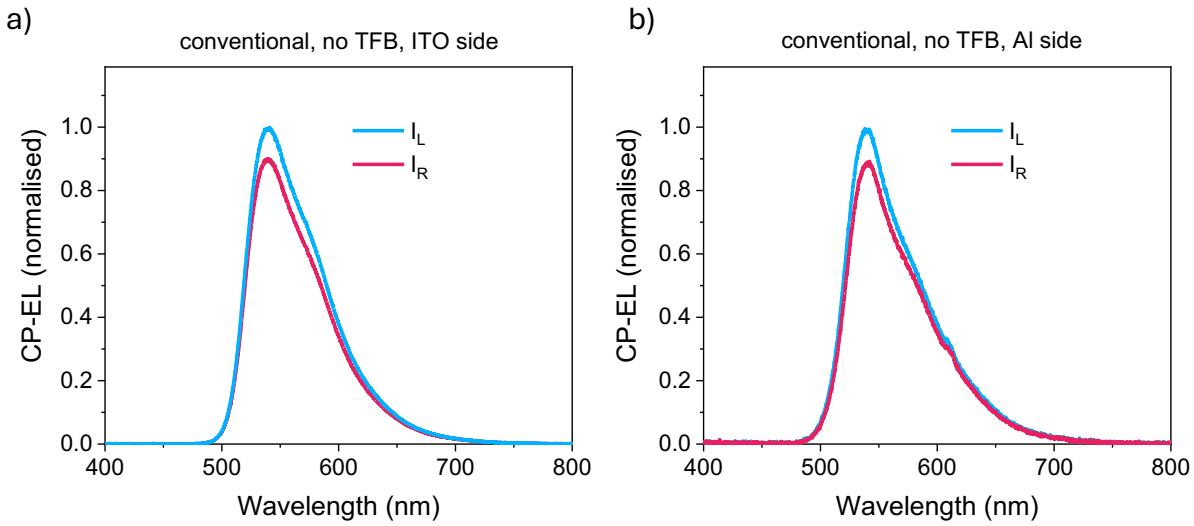

Figure S33: CP-EL of conventional CP-OLEDs without HTL and semi-transparent top electrode (20 nm Al), measured from different device sides.

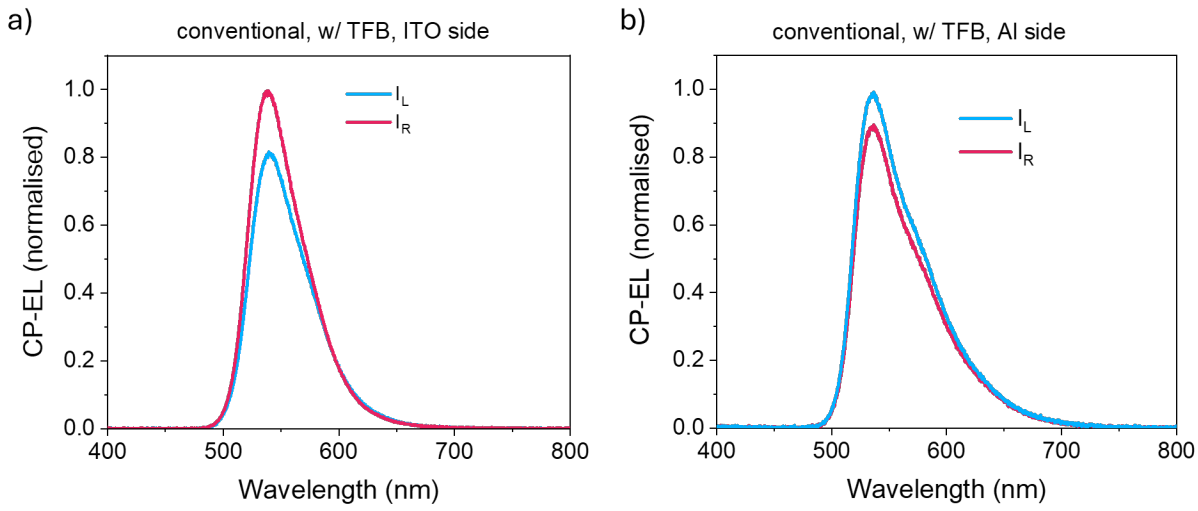

Figure S34: CP-EL of conventional CP-OLEDs with TFB as HTL and semi-transparent top electrode (20 nm Al), measured from different device sides.

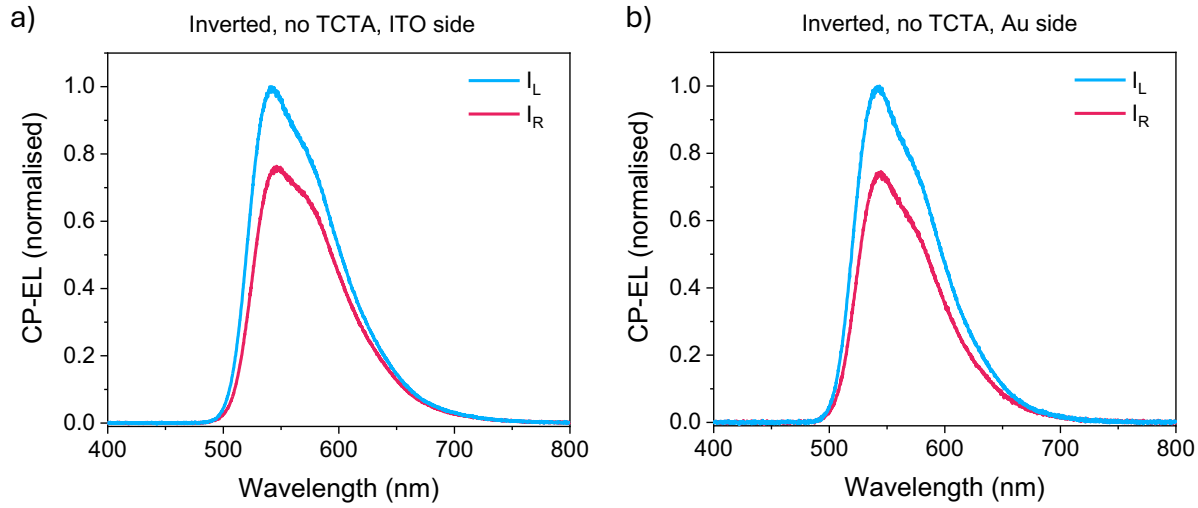

Figure S35: CP-EL of inverted CP-OLEDs without HTL and semitransparent top electrode (20 nm Au), measured from different device sides.

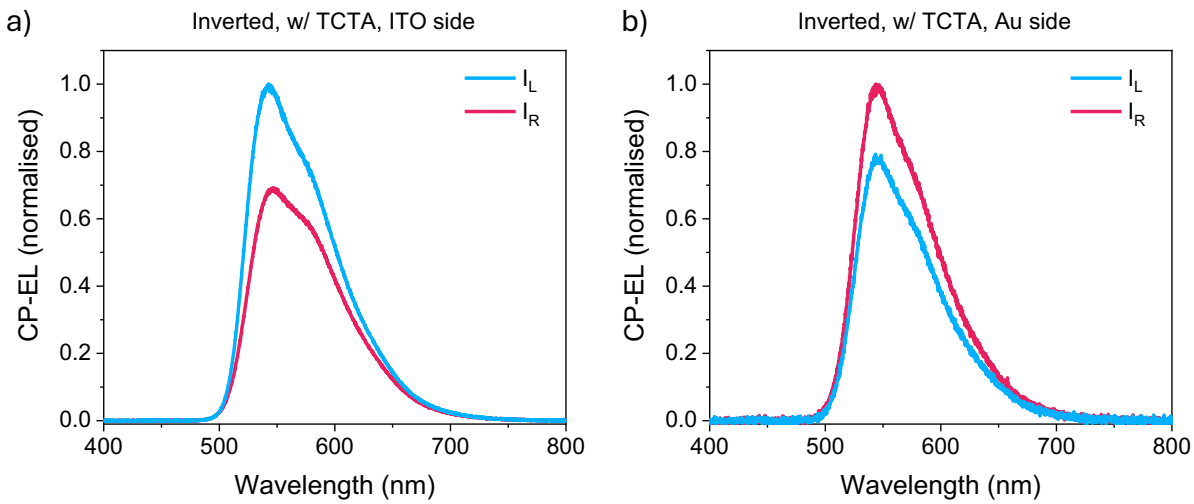

Figure S36: CP-EL of inverted CP-OLEDs with TCTA as HTL and semitransparent top electrode (20 nm Au), measured from different device sides.

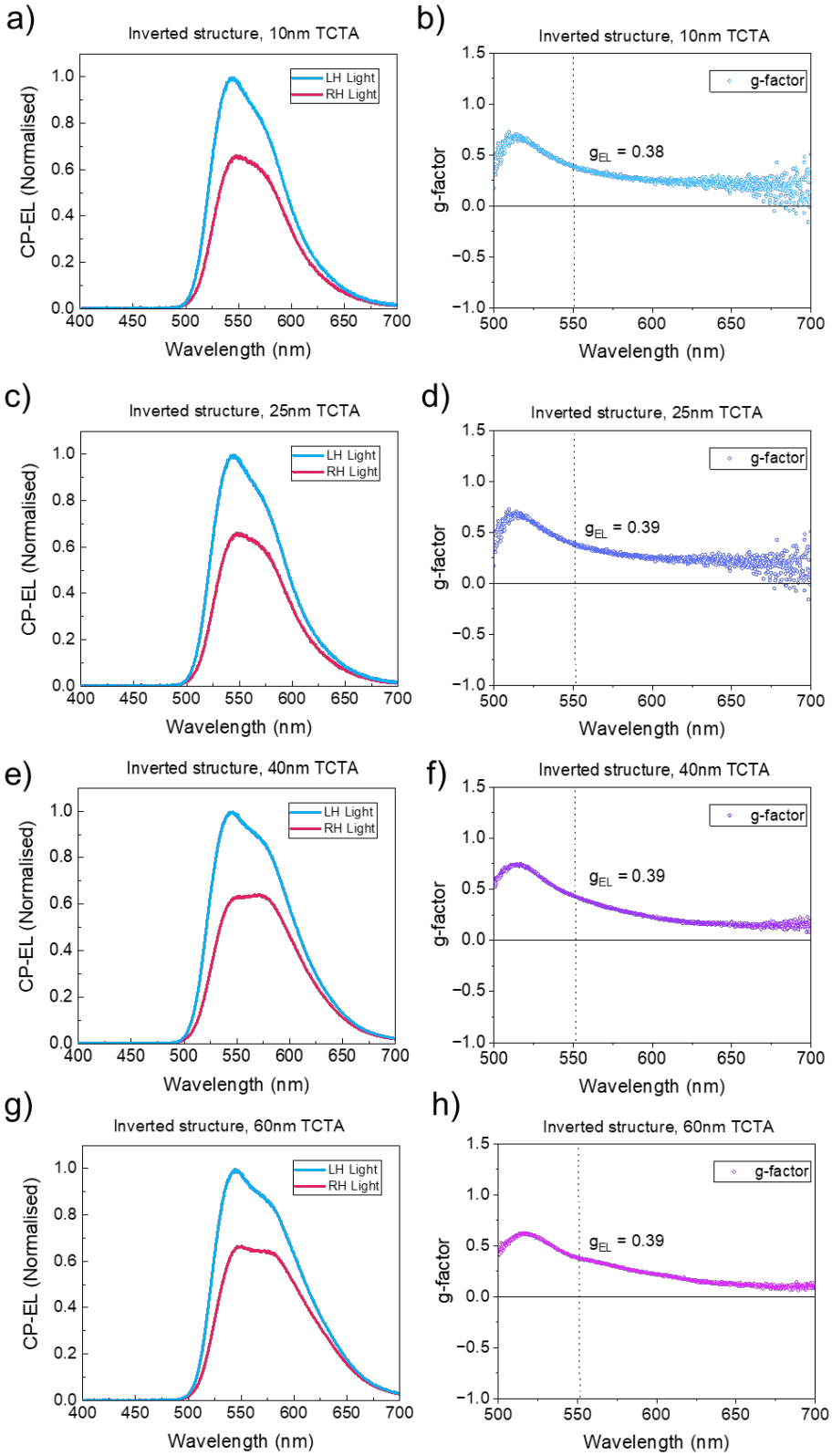

Figure S37: CP-EL and g_{EL} of inverted CP-OLEDs with different thicknesses of TCTA a) CP-EL with 10 nm of TCTA b) g_{EL} with 10 nm of TCTA c) CP-EL with 25 nm TCTA d) g_{EL} with 25 nm TCTA e) CP-EL with 40 nm TCTA f) g_{EL} with 40nm of TCTA g) CP-EL with 60 nm of TCTA h) g_{EL} with 60 nm TCTA

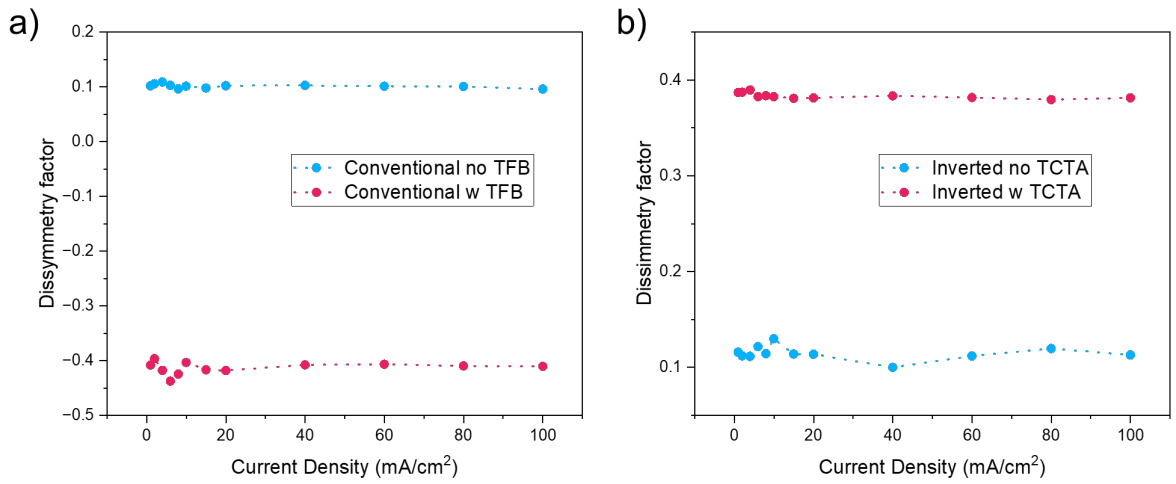

Figure S38: g_{EL} of CP-OLEDs with different device architectures as a function of current density.

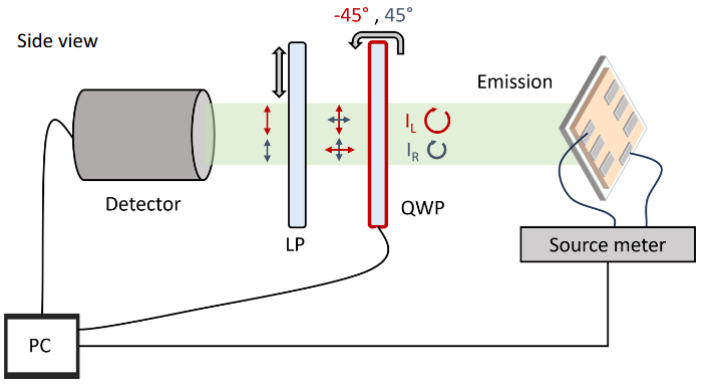

Figure S39: Scheme of CP-EL experimental setup.

Supplementary note S1: Circularly polarised light and orbital angular momentum

If CPL is emitted along an axis, CPL emission can be derived as:

$$I_{\mathrm{L}} - I_{\mathrm{R}} = ACPE + NCPE = -\frac{2\pi e^2}{\hbar} I_0 \mathrm{Im}[x^{01} y^{10}]\delta - \frac{2\pi e}{\hbar c} I_0 \mathrm{Im}[m_x^{01} x^{10} + m_y^{01} y^{10}]\delta$$

With $x^{01} = \langle 0|x|1\rangle$ electric transition dipole, $m_x^{01} = \langle 0|m_x|1\rangle$ magnetic transition dipole, $\delta = \delta(\epsilon_1 - \epsilon_0 - \hbar\omega)$ with $\epsilon_{1/0}$ energy of the excited and ground states and $\hbar\omega$ the photon energy.

The full derivation of CPL emission follows Fermi's golden rule and can be found in previous work[11].

NCPE (Normal circularly polarised emission)

The term for NCPE $\left(-\frac{2\pi e}{\hbar c} I_0 \mathrm{Im}[m_x^{01} x^{10} + m_y^{01} y^{10}]\delta\right)$ corresponds to the natural chiroptical activity and describes CD, CPPL and CP-EL in conventional systems. Because during the optical transition, the change in the orbital angular momentum is zero, emitted photons in opposite directions must carry opposite spins, therefore having the same handedness. In other words, emitted photons carrying opposite spins and propagating in opposite directions give rise to CPL with the same sign.

ACPE (anomalous circularly polarised emission)

The term for ACPE describes the dipole interaction with the light electric field. This term is usually zero if it respects time-reversal symmetry. However, when an electrical current is flowing in a chiral material, electrons and holes flowing in the material can induce orbital magnetisation, breaking time-reversal symmetry.

Considering the optical transition for light emission, the term can be rewritten as:

$$I_{\mathrm{L}} - I_{\mathrm{R}} = -\frac{2\pi e^2}{\hbar} I_0 \mathrm{Im}[x^{01} y^{10}]\delta = \frac{\pi e^2}{m_e \hbar \omega} \langle \hat{L_z} \rangle_{0\to 1} \delta(\epsilon_1 - \epsilon_0 - \hbar\omega)$$

This term is typically zero if time-reversal symmetry is obeyed. When time-reversal symmetry is broken, this term cannot be neglected, and there is a finite probability of emitting photons with the same spin propagating in opposite directions. This gives rise to CPL with opposite sign.

With $\langle \hat{L_z} \rangle_{0\to 1} = \langle 0|x|1\rangle\langle 1|p_y|0\rangle - \langle 0|y|1\rangle\langle 1|p_x|0\rangle = x^{01} p_y^{10} - y^{01} p_x^{10}$, expectation value for the state $|0\rangle$ and p linear momentum $p_{x/y} = -i\hbar \frac{\partial}{\partial x/y}$.

Supplementary note S2: Angular momentum transfer from charges to light

In this work, $\Delta l = l_e - l_h$ and is inherited from the orbital angular momentum of the recombining electron-hole pair, formed in a chiral material, with CPL being dependent on the emission direction. The different possibilities are:

- The recombination zone is in the middle of the device. In this case, holes and electrons carry the same orbital angular momentum $+l_e$ and $+l_h$. The total orbital angular momentum of the exciton will be $\Delta l = l_e - l_h$, with $+l_e \approx +l_h$, therefore $\Delta l = 0$ and the time reversal symmetry is respected, with the emission mechanism being NCPE. This is also current-direction independent.
- The recombination zone is close to one of the interfaces with the transport layers of the device. In this case, only one type of charge carrier carries angular momentum $\pm l_e$ ($\pm l_h$). The other type of charge carrier does not carry orbital angular momentum, therefore $\Delta l = \pm l_e (\pm l_h)$. The sign of Δl is current-dependent and changes sign upon reversing the current direction (i.e. inverting the device architecture).

In ACPE, when the emission is current-direction dependent, the finite angular momentum transfer to the photon spin generates the emission of opposite handedness of CPL from the opposite side of the CP-OLED.

$$\Delta l = \langle \hat{L_z} \rangle_{0\to1} = x^{01} p_y^{10} - y^{01} p_x^{10}$$

The direction of the current forces different handedness of CPL for opposite emission direction, and reversing when the current is reversed.

Supplementary note S3: Optical Losses

In both cases, when NCPE and ACPE are active in a device, optical losses can lead to a lower dissymmetry factor than theoretically possible.

Considering the previous model previously developed by Zinna et al[12], NCPE contributions to the dissymmetry factor must be added to ACPE.

If we assume the same approximation as the previous model, the light polarisation emitted from a conventional device where the RZ is close to the transparent electrode (i.e., x=0) can be evaluated using the following scheme:

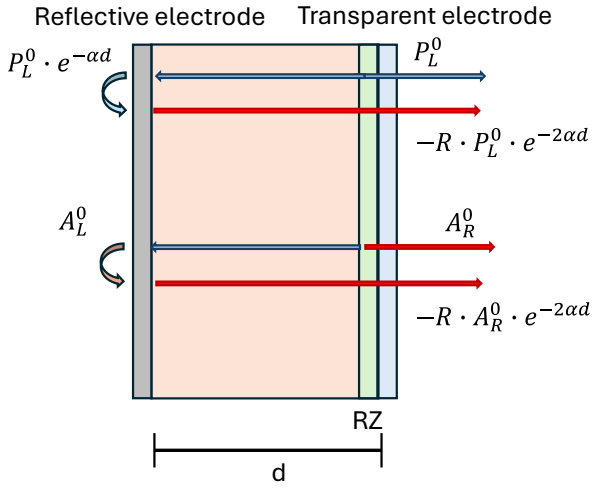

The final g_{EL} of the device would be calculated considering the left-handed and right-handed light emission from the emissive layer as:

$$I'_L = P_L^0 + R \cdot P_R^0 \, e^{-2\alpha d} + A_R^0(1 + R \cdot e^{-2\alpha d})$$

$$I'_R = P_R^0 + R \cdot P_L^0 \, e^{-2\alpha d} + A_L^0(1 + R \cdot e^{-2\alpha d})$$

Where:

I'_L is the total intensity of left-handed polarisation component emitted by the chiral emissive species

I'_R is the total intensity of left-handed polarisation component emitted by the chiral emissive species

P_L^0 is the intrinsic intensity of left-handed polarisation emitted via NCPE by the emissive species

P_R^0 is the intrinsic intensity of right-handed polarisation emitted via NCPE by the emissive species

R is the total reflectivity of the reflective electrode

α is the attenuation coefficient

d is the total emissive layer thickness

A_R^0 is the intensity of right-handed polarisation emitted via ACPE by the emissive species

A_L^0 is the intensity of left-handed polarisation emitted via ACPE by the emissive species

The predicted g_{EL} from the devices in which NCPE and ACPE are contributing to CP emission could be calculated as:

$$g_{EL} = 2\frac{I'_L - I'_R}{I'_L + I'_R}$$

Which, expanded, gives:

$$g_{EL} = 2\frac{P_L^0 + R \cdot P_R^0\, e^{-2\alpha d} + A_R^0(1 + R \cdot e^{-2\alpha d}) - P_R^0 - R \cdot P_L^0\, e^{-2\alpha d} - A_L^0(1 + R \cdot e^{-2\alpha d})}{P_L^0 + R \cdot P_R^0\, e^{-2\alpha d} + A_R^0(1 + R \cdot e^{-2\alpha d}) + P_R^0 + R \cdot P_L^0\, e^{-2\alpha d} + A_L^0(1 + R \cdot e^{-2\alpha d})}$$

Furthermore, in real systems where the recombination zone is not an infinitesimally small line, the NCPE component should be calculated considering the total recombination zone thickness:

$$g_{EL} = \int_0^y g_{PL}^0 \frac{1 - Re^{-\alpha d}}{1 + Re^{-\alpha d}} \rho(y) dy \ ,$$

with *d* layer thickness and x position of the RZ with respect to the transparent electrode and integrated over the thickness (y) of the recombination zone.

Comparative table of literature

Emissive Material	Category (i.e. polymer, small molecule, inorganic)	Efficiency (Current efficiency Cd/A or EQE %)	Dissymmetry factor with optical excitation g_{PL}	Dissymmetry factor in devices (g_{EL})	Comments
Inorganic					
$CsPbBr_3$ [13]	Metal Halide Perovskite emitter	5.47%	/	0.24	Spin injection via chiral shell in core-shell nanocrystals
$MAPbBr_3$ [14]	Metal Halide Perovskite emitter	3.6%	5.6×10^{-3}	0.18	Spin injection via ligand modification of perovskite NCs
$CsPb(I_{1-x}Br_X)_3$ [15]	Metal-Halide perovskite nanocrystals	11%	/	5.2×10^{-2}	Spin Injection via chiral perovskite
CdSe/ZnS [16]	Inorganic Quantum dots	2.7%	/	1.6×10^{-2}	Spin injection via chiral perovskite
CdSe/ZnS [17]	Inorganic quantum dots	20.39%	0.31	0.24	Spin injection via chiral MOF
$(Al_{0.32}Ga_{0.68})_{0.5}In_{0.5}P$ [18]	Inorganic Quantum Well	/	/	0.3	Spin injection via chiral perovskite
Organic Small molecules					
(±)-**1** [19]	Chiral Phosphorescent emitter	0.49 cd A^{-1}	0.22	0.38	Chiral Phosphorescent emitter
(R/S)-Pt [20]	Chiral phosphorescent emitter	11.3%	2×10^{-2}	6×10^{-2}	Chiral metal complex, dissymmetry enhanced via formation of liquid crystal (functionalisation with mesogenic groups)

(R/S)-ZnL [21]	Chiral Phosphorescent emitter	0.04 cd/A	3×10^{-3}	1.5×10^{-2}	Chiral metal complex
(R/S)-Cz-Ax-CN [22]	Chiral TADF emitter	12.7%	4.8×10^{-3}	1.4×10^{-2}	Chiral TADF small molecule, dissymmetry factor enhanced by aggregated induced emission
(R/S)-BN-AF [23]	Chiral TADF emitter	1.5%	2×10^{-2}	9.1×10^{-2}	Chiral TADF small molecule, dissymmetry factor enhanced by aggregated induced emission
$CsEu(hfbc)_4$ [12]	Chiral Lanthanide	5×10^{-3} %	1.38	-1 (semitransparent)	Chiral Lanthanides, dissymmetry enhanced via fabrication of semitransparent devices and optimisation of the Recombination zone position
$Eu(TTA)_3{}^{i}PrPyBox$ [24]	Chiral Lanthanide	1.01%	0.53	0.63	Chiral Lanthanides, dissymmetry enhanced via fabrication of semitransparent devices
Organic polymers					
C-522 [25]	Polymer with chiral sidechain	0.94 Cd/A	0.72	0.35	Chiral polymers with dissymmetry induced by

					chiral sidechains
c-FPBT [26]	Polymer with chiral sidechains	//	0.6	0.6	Dissymmetry due to formation of cholesteric film
F8BT + (*P*/*M*)-aza[6]H [27]	Polymer with chiral additive	//	0.23	0.2	Chiral phase induced by doping with a chiral additive an achiral polymer
F8BT + R5011 [28]	Polymer with chiral additive	4.46 cd/A	0.72	1.13	Alignment layers exploited to align the polymer, CP emission achieved via structural chirality
F8BT + aza[6]H [29]	Polymer with chiral additive	4.0 cd/A	0.35	-1.05	Handedness controlled via thickness of the active layer
$(F8BT)_{0.9}$-$(R\text{-}5011)_{0.1}$-$(DBN\text{-}ICZ)_{0.005}$ [30]	Polymer with chiral additive	4.6%	0.26	0.16	Chiral co-assembly, with energy transfer from chiral host to chiral acceptor. The handedness is defined by the chirality of host
(*R*)-BN-MDPA: CBP: cPF8PhO8 [31]	Chiral polymer with Chiral TADF emitter as dopant	0.18%	1.4×10^{-2}	9.1×10^{-2}	Dissymmetry enhanced via energy-transfer from chiral host to chiral guest
F8BT:aza[6]H (previous work) [11]	Chiral polymer with chiral additive	//	0.38	Conventional devices: 0.53	CP-EL handedness is controlled via the

				Inverted Devices: -0.33	inversion of the electric field direction
F8BT:monoF[6]H (This Work)	**Polymer with chiral additive**	**Conventional NCPE: 1.25 cd/A** **Inverted NCPE: 4.3 cd/A** **Conventional ACPE: 4.7 cd/A** **Inverted ACPE: 12.9 cd/A**	**0.24**	**Conventional NCPE: 0.10** **Inverted NCPE: 0.13** **Conventional ACPE: -0.40** **Inverted ACPE: 0.38**	**CP-EL emission mechanism controlled via charge-carrier balance. Balanced charge recombination leads to NCPE (reciprocal emission); unbalanced charge recombination leads to ACPE (non-reciprocal emission). Handedness can be controlled without inverting the electric field direction**

Table S5: Comparison table of literature

References

1. Geny, A. *et al.* Air-stable {(C5H5)Co} catalysts for [2+2+2] cycloadditions. *Angewandte Chemie - International Edition* **48**, 1810–1813 (2009).
2. Hack, D. *et al.* Asymmetric Synthesis of Spiropyrazolones by Sequential Organo- and Silver Catalysis. *Angewandte Chemie - International Edition* **55**, 1797–1800 (2016).
3. Frisch, M. J.; Trucks, G. W.; Schlegel, H. B.; Scuseria, G. E.; Robb, M. A.; Cheeseman, J. R.; Scalmani, G.; Barone, V.; Petersson, G. A.; Nakatsuji, H.; Li, X.; Caricato, M.; Marenich, A. V.; Bloino, J.; Janesko, B. G.; Gomperts, R.; Mennucci, B.; Hratch, Inc. Gaussian 16, Revision A.03. Preprint at (2016).
4. Ernzerhof, M., Burke, K. & Perdew, J. P. Long-range asymptotic behavior of ground-state wave functions, one-matrices, and pair densities. *Journal of Chemical Physics* **105**, 2798–2803 (1996).
5. Kendall, R. A., Dunning, T. H. & Harrison, R. J. Electron affinities of the first-row atoms revisited. Systematic basis sets and wave functions. *J Chem Phys* **96**, 6796–6806 (1992).
6. Grimme, S., Antony, J., Ehrlich, S. & Krieg, H. A consistent and accurate ab initio parametrization of density functional dispersion correction (DFT-D) for the 94 elements H-Pu. *Journal of Chemical Physics* **132**, (2010).
7. Miertuš, S., Scrocco, E. & Tomasi, J. Electrostatic interaction of a solute with a continuum. A direct utilizaion of AB initio molecular potentials for the prevision of solvent effects. *Chem Phys* **55**, 117–129 (1981).
8. Miertuš, S. & Tomasi, J. Approximate evaluations of the electrostatic free energy and internal energy changes in solution processes. *Chem Phys* **65**, 239–245 (1982).
9. Hussain, R., Jávorfi, T. & Siligardi, G. CD Imaging at High Spatial Resolution at Diamond B23 Beamline: Evolution and Applications. *Front Chem* **9**, 616928 (2021).
10. Fong, H. H., Papadimitratos, A., Hwang, J., Kahn, A. & Malliaras, G. G. Hole Injection in a Model Fluorene–Triarylamine Copolymer. *Adv Funct Mater* **19**, 304–310 (2009).
11. Wan, L., Liu, Y., Fuchter, M. J. & Yan, B. Anomalous circularly polarized light emission in organic light-emitting diodes caused by orbital–momentum locking. *Nat Photonics* **17**, 193–199 (2022).
12. Zinna, F. *et al.* Design of Lanthanide-Based OLEDs with Remarkable Circularly Polarized Electroluminescence. *Adv Funct Mater* **27**, (2017).
13. Jang, G. *et al.* Core–Shell Perovskite Quantum Dots for Highly Selective Room-Temperature Spin Light-Emitting Diodes. *Advanced Materials* **36**, 2309335 (2024).
14. Yang, C. H. *et al.* In Situ Formed Perovskite Nanocrystal Films Toward Efficient Circularly Polarized Electroluminescence. *Adv Funct Mater* **34**, 2310500 (2024).

15. Kim, Y.-H. *et al.* Chiral-induced spin selectivity enables a room-temperature spin light-emitting diode. *Science* **371**, 1129–1133 (2021).

16. Wang, Q. *et al.* Spin Quantum Dot Light-Emitting Diodes Enabled by 2D Chiral Perovskite with Spin-Dependent Carrier Transport. *Advanced Materials* **36**, 2305604 (2023).

17. Mustaqeem, M. *et al.* Solution-Processed and Room-Temperature Spin Light-Emitting Diode Based on Quantum Dots/Chiral Metal-Organic Framework Heterostructure. *Adv Funct Mater* **33**, 2213587 (2023).

18. Hautzinger, M. P. *et al.* Room-temperature spin injection across a chiral perovskite/III–V interface. *Nature 2024* **631**, 307–312 (2024).

19. Brandt, J. R., Wang, X., Yang, Y., Campbell, A. J. & Fuchter, M. J. Circularly Polarized Phosphorescent Electroluminescence with a High Dissymmetry Factor from PHOLEDs Based on a Platinahelicene. *J Am Chem Soc* **138**, 9743–9746 (2016).

20. Qian, G. *et al.* Chiral Platinum-Based Metallomesogens with Highly Efficient Circularly Polarized Electroluminescence in Solution-Processed Organic Light-Emitting Diodes. *Adv Opt Mater* **8**, 2000775 (2020).

21. Chen, Y. *et al.* Strong circularly polarized electroluminescence based on chiral salen-Zn(ii) complex monomer chromophores. *Mater Chem Front* **3**, 867–873 (2019).

22. Li, M., Wang, Y. F., Zhang, D., Duan, L. & Chen, C. F. Axially Chiral TADF-Active Enantiomers Designed for Efficient Blue Circularly Polarized Electroluminescence. *Angewandte Chemie - International Edition* **59**, 3500–3504 (2020).

23. Song, F. *et al.* Highly Efficient Circularly Polarized Electroluminescence from Aggregation-Induced Emission Luminogens with Amplified Chirality and Delayed Fluorescence. *Adv Funct Mater* **28**, 1800051 (2018).

24. Zinna, F. *et al.* Modular chiral Eu(iii) complexes for efficient circularly polarized OLEDs. *J Mater Chem C Mater* **10**, 463–468 (2022).

25. Geng, Y. *et al.* Origin of Strong Chiroptical Activities in Films of Nonafluorenes with a Varying Extent of Pendant Chirality. *J Am Chem Soc* **125**, 14032–14038 (2003).

26. Di Nuzzo, D. *et al.* High Circular Polarization of Electroluminescence Achieved via Self-Assembly of a Light-Emitting Chiral Conjugated Polymer into Multidomain Cholesteric Films. *ACS Nano* **11**, 12713–12722 (2017).

27. Yang, Y., Da Costa, R. C., Smilgies, D. M., Campbell, A. J. & Fuchter, M. J. Induction of circularly polarized electroluminescence from an achiral light-emitting polymer via a chiral small-molecule dopant. *Advanced Materials* **25**, 2624–2628 (2013).

28. Lee, D.-M., Song, J.-W., Lee, Y.-J., Yu, C.-J. & Kim, J.-H. Control of Circularly Polarized Electroluminescence in Induced Twist Structure of Conjugate Polymer. *Advanced Materials* **29**, 1700907 (2017).

29. Wan, L. *et al.* Inverting the Handedness of Circularly Polarized Luminescence from Light-Emitting Polymers Using Film Thickness. *ACS Nano* **13**, 8099–8105 (2019).

30. Guo, C. H. *et al.* Chiral Co-Assembly with Narrowband Multi-Resonance Characteristics for High-Performance Circularly Polarized Organic Light-Emitting Diodes. *Advanced Materials* **36**, 2406550 (2024).

31. Moreno-Naranjo, J. M. *et al.* Enhancing Circularly Polarized Electroluminescence through Energy Transfer within a Chiral Polymer Host. *Advanced Materials* 2402194 (2024)